Surface oxygen vacancy enhanced the activation of peroxymonosulfate on α-Ni$_{0.2}$Fe$_{1.8}$O$_3$ for water decontamination: The overlooked role of H$_2$O in interface mechanism

Shuyu Wang, Jing Kang, Pengwei Yan [*], Jimin Shen, Jinxiang Zuo, Yizhen Cheng, Linlu Shen, Binyuan Wang, Shengxin Zhao, Zhonglin Chen [*]

State Key Laboratory of Urban Water Resources and Environment, School of Environment, Harbin Institute of Technology, Harbin 150090, PR China

ARTICLE INFO

ABSTRACT

Oxygen vacancies (OVs)-rich α-Ni$_{0.2}$Fe$_{1.8}$O$_3$ with dual metal sites was synthesized by Ni^{2+} isomorphously substituted α-Fe$_2$O$_3$ to activate peroxymonosulfate (PMS) for aceclofenac (ACF) degradation. A novel insight was proposed for the overlooked role of H$_2$O in the surface-complexed process between PMS and unsaturated metal sites induced by OVs. The surface-bond SO$_4^{\bullet-}$ and •OH were demonstrated as the dominant reactive oxygen species (ROS). In situ ATR and Raman spectra revealed the reaction of HSO$_5^-$ with the surface metal sites by replacing the surface-bonded -OH. The DFT study revealed the spontaneous formation of hydrolyzed -OH on OVs (ΔG=−1.45 eV), which was further replaced by HSO$_5^-$ to complex with metal sites (ΔG=−3.58 eV). The O$_I$ of the H-O$_I$-O$_{II}$-SO$_3$ was more readily bonded with the Ni or Fe sites around OVs, causing the O-O cleavage for SO$_4^{\bullet-}$ generation. This study proposed a brand-new perspective for the interfacial behavior of PMS activation.

1. Introduction

Sulfate radicals based advanced oxidation technologies (SR-AOTs), especially peroxymonosulfate (PMS) activation, have gained remarkable attention and extensively investigated in water treatment, due to the high oxidation potential (2.5–3.1 V), non-selectivity, extensive pH adaptability, longer lifetime of SO$_4^{\bullet-}$ (30–40 μs) [1]. Various activation strategies of PMS have been sufficiently explored, including UV activation [2], heat activation [3], alkaline activation [4], carbonaceous materials [5] and transition metal activation. Heterogeneous activation of PMS by transition metal oxides (TMO) with multiple valence states was widely used based on its advantages of less energy input, specific pH conditions, high efficiency and excellent recovery performance [6]. Nevertheless, safety and cost severely limited the application of catalysts.

Iron and copper based catalysts are widely used for the activation of oxidants containing peroxide bonds due to their high catalytic performance, such as zerovalent iron [7], zerovalent copper [8] and their metal oxides [9]. As an essential element of the human body, iron is non-toxic and harmless, and widely distributed on earth. Hematite (α-Fe$_2$O$_3$), possessing the most stable crystal structure and

thermodynamically stable n-type semiconducting properties among iron ore, has received widespread attention in water purification, for catalyzing ozonation [10], photocatalysis [11], electro-Fenton process [12] and UV [13]. However, the poor catalytic performance of α-Fe$_2$O$_3$ for PMS restricted its application in this field.

Oxygen vacancies (OVs) have been evidenced that play a crucial role in tuning physical and chemical properties of metal oxides, such as energy levels, d^0 ferromagnetism, electrical conductivity, redox property and catalytic efficiency [14–16]. It can also act as a reaction site on the catalyst surface, accelerating the electrons transfer from it to the surface-complexed oxidant [17], thus mediating the generation of reactive oxidative species (ROS). With the deepening of research, there has been application in constructing OVs on TMO to improve the catalytic performance in activating O$_3$ [18], H$_2$O$_2$ [19] and PMS [20]. However, the activation mechanisms in these fields were not unified and clear, especially in PMS activation. Ndayiragije et al. proposed that OVs accelerated the activation of PMS by enhancing the redox cycling of Mn^{4+}/Mn^{3+} rather than Mn^{3+}/Mn^{2+} in MnO$_2$, emphasizing the effect of OVs on local metal ions [20]. Whereas Lei et al. reported that the electron transfer from Co-Ov-PMS and PMS-Co-Ov triggered the radical and nonradical pathway, respectively, indicating the electron transfer

intermediate role of OVs [21]. Nevertheless, Guo et al. raised that OVs enhancing activation of PMS mainly attributed to the facilitating of PMS adsorption and electron transfer [22]. Although the mechanisms proposed in recent reports are different, they are all based on the adsorption of PMS on OVs. However, the surface-complexed way and bond sites of PMS to OVs have not been seriously considered, which is the prerequisite and key step in the activation process. Especially the role of H_2O molecules in this process, which are much more numerous than PMS in water-based surroundings and readily contact the OVs on the catalyst surface, has been overlooked for a long time. Besides, the bonded-OH groups from H_2O dissociation were reported to increase the electron density of transition metals and act as σ-donor ligands, which might greatly affect PMS activation [23]. Thus, the role of H_2O in the interaction of PMS with OVs must be evaluated. α-Fe_2O_3 possesses the characteristic of being rich in terminal hydroxyl groups, which surface is prone to water adsorption and dissociation [24]. Therefore, introducing OVs to α-Fe_2O_3 was not only expected to improve its catalytic performance, but also helpful for exploring the role of H_2O in interface mechanism.

The doping strategy in metal oxides for OVs construction has emerged rapidly due to its simplicity and flexibility [25]. Generally, doping of metal elements could enhance the mechanical strength and simultaneously reduce the ions leaching of TMO in application [26]. Nevertheless, due to the varied radius and valence of the doped ions, it might cause relatively low crystallinity and even deconstruction of the host metal oxides [27], which is prone to ion dissolution and not conducive to exploring the activation mechanism. Meaning the dopants should be distinguished during the synthesis process. Inspired by hematite often containing isomorphic substitution of Ti, Al, Mn in nature, we aimed to synthesize the isomorphic substituted α-Fe_2O_3 in this study. Based on the Hume-Rothery rules, when the radius of the doped ions is close to the host metal ions (the difference was within 15%), the original crystal structure can be maintained by the isomorphous substitution process [28]. Additionally, doping a low valance metal ion more readily formed OVs due to the imbalance of the total charge [22,29]. Due to the similar radius (r_{Ni}^{2+}=0.069 nm, r_{Fe}^{3+}=0.064 nm, Δ=7.8%<15%) and the relatively lower valance of Ni^{2+} than Fe^{3+}, Ni^{2+} was taken into consideration. In the sight of previous studies, a series of nickel (Ni) oxides and single-Ni-atom presented an excellent catalytic performance for PMS due to redox cycle of Ni^{2+} and Ni^{3+} [30,31]. Therefore, Ni^{2+} was designed to dope in α-Fe_2O_3 to construct OVs and dual-metal active sites in the structure to activate PMS.

Aceclofenac (ACF), as an emerging anti-inflammatory drug to safely substitute the banned vulture-killing diclofenac (DCF) [32], was recently found to be rapidly metabolized into DCF by livestock and then released into the environment, which still seriously threaten the survival of vultures [33]. So far, the research on ACF is still limited in the establishment of detection methods and identification in the water environment [34], and the effective degradation of ACF and corresponding degradation pathway in water are still blank. Therefore, SR-AOTs can be tried as an effective means for the removal of ACF.

This study aimed to uncover the catalytic mechanism of OVs for PMS activation, particularly to make clear the role of H_2O in the interfacial reaction between PMS and catalyst. Hence, the Ni^{2+} isomorphously substituted α-Fe_2O_3 material with OVs was first synthesized for activation of PMS to degrade ACF. And the present study investigated 1) the formation mechanism of OVs via Ni^{2+} substitution process in α-Fe_2O_3 structure, 2) the catalytic efficiency of the as-synthesized catalyst for PMS activation, 3) the activation mechanism of the surface-complexed PMS by OVs for ROS generation, 4) the influence of different OVs contents on the activation of PMS, 5) degradation mechanism of ACF. In these processes, the in-situ ATR and Raman spectra of HSO_5^- and SO_4^{2-} in water and the process of how HSO_5^- replaced surface -OH bonded to unsaturated metal sites and decomposed into surface-absorbed $SO_4^{\bullet-}$ was confirmed by DFT study for the first time. Finally, a novel interfacial mechanism was proposed for OVs-induced PMS activation.

2. Material and methods

2.1. Chemicals and reagents

Aceclofenac (ACF, ≥ 95%) , ethanol (EtOH, gradient grade), *tert*-butanol (TBA, 99.5%), furfuryl alcohol (FFA, 98%), chloroform (CF, 98%), 5, 5-dimethyl-1-pyrroline-N-oxide (DMPO, ≥97%) and 2,2,6,6-tetramethylpiperidine (TEMP, 95%) were purchased from Macklin. Peroxymonosulfate (PMS), diclofenac (DCF, ≥97%), meclofenamic acid (MCF, ≥97%), sulfamethoxazole (SMX, ≥95%), carbamazepine (CBZ, ≥98%), diatrizoic acid (DTZ, ≥98%), nitrobenzene (NB, ≥99.5%), benzoic acid (BA, ≥99.5%), phenol (PE, ≥99.5%), 4-chlorophenol (4-CP), 2,4-dichlorophenol (2,4-DCP, ≥99.7%) and bisphenol A (BPA, ≥99.0%) were obtained from Merck. $Fe(NO_3)_3 \bullet 9 H_2O$ (≥97%), Ni $(NO_3)_2 \bullet 6 H_2O$ (≥97%), $NH_3 \bullet H_2O$ (28 wt, 100%), NaOH (98%), HNO_3(65%) and citric acid (98%) were supplied by J&K Scientific Co., Beijing, China. Other chemicals used in the experiment were of analytic reagent grade. All the solutions were prepared with Milli-Q water.

2.2. Synthesis and characterization of catalysts

The Ni^{2+} doped α-Fe_2O_3 was prepared via the precipitation-calcination method with $Fe(NO_3)_3 \bullet 9 H_2O$ and $Ni(NO_3)_2 \bullet 6 H_2O$ as precursors. Firstly, the $Ni(NO_3)_2 \bullet 6 H_2O$ and $Fe(NO_3)_3 \bullet 9 H_2O$ (1 M) with planned molar ratio (5%, 10%, 20%, 30%) were dissolved in the Milli-Q water (100 mL), and then the $NH_3 \bullet H_2O$ was added to the stirring mixture dropwise to adjust the solution pH to 11, and precipitation was formed in the process. The suspension was sealed and aged at 60 ℃ for 72 h. After that, the precipitation was separated by filtration, washed, and dried at 60 ℃. Finally, the solids were calcinated at 400 ℃ for 2 h, ground and sieved. The as-prepared catalysts with specific Ni/Fe molar ratios were named α-$Ni_{0.1}Fe_{1.9}O_3$, α-$Ni_{0.2}Fe_{1.8}O_3$, α-$Ni_{0.4}Fe_{1.6}O_3$ and α-$Ni_{0.6}Fe_{1.4}O_3$, respectively. As a reference, the α-Fe_2O_3 was synthesized in the same procedure without the addition of $Ni(NO_3)_2 \bullet 6 H_2O$.

The detailed characterization of catalysts was shown in Text S1.

2.3. Experimental procedures

Degradation of pollutants was conducted in 250 mL beakers in parallel at room temperature. ACF, catalysts and PMS were added simultaneously to start the reaction under a mediate stirring speed. The sample was collected at specific time intervals and quenched immediately with $NaNO_2$ (0.1 M), then filtered by 0.22 μm membranes before analysis. The adsorption removal process of ACF was carried out by adding catalysts alone. The solution pH was adjusted by 0.1 M NaOH or HNO_3 solution. The quenching tests were performed with the presence of TBA, EtOH, CF, FFA and KI in the reaction system together with ACF. Interfacial reactions were revealed via in situ ATR-FTIR and Raman processes, as shown in Text S2.

2.4. Electrochemical tests

Electrochemical analysis tests were performed in 1 M KCl solution with a three-electrode-cell configuration by an electrochemical workstation (auto lab PGSTAT302N, Metrohm), including a working electrode (glassy carbon electrode coated by catalysts), a counter electrode (platinum electrode), and a reference electrode (Ag/AgCl). The cyclic voltammetry (CV) tests were recorded between –0.1 V and +1.0 V with a scan rate of 10 mV/s. Electrochemical impedance spectroscopy (EIS) analysis was conducted by sweeping the frequency from 125,000 to 0.1 Hz. The open-circuit potential (OCP) tests were monitored by chronopotentiometry analysis, and PMS or ACF was added to the electrolytic cell at a certain reaction time.

2.5. Analysis methods

The concentrations of the target contaminants were detected by a UHPLC (Agilent, 1290) with a C18 column (ACQUITY BEH, 2.1 × 100 mm, 1.7 μm). The UV detection wavelength and the mobile phase for each contaminant were listed in Table S1. The total organic carbon (TOC) was detected by an Analytik Jena Multi N/C 2100 s analyzer. The residual PMS was measured according to the method described, as shown in Text S3. The intermediates of ACF were determined using the UHPLC-QTOF/MS (Agilent, USA) with an ACQUITY BEH C18 column (2.1 ×100 mm, 1.7 μm), details were shown in Text S4.

2.6. Theoretical calculations

The optimized structures of ACF and the products based on the density functional theory (DFT) calculation were conducted on the Gaussian 09 W program at the B3LYP/6–31 G level and analyzed by Multiwfn. The calculation-simulated FTIR and Raman models of HSO_5^- and SO_4^{2-} were obtained at B3LYP/6–311 +G(2df,2p) [35]. The electronic structure and interface adsorption energy of HSO_5^- and H_2O on reactive sites were calculated via the Materials studio Castep function package, details were listed in Text S5.

3. Results and discussion

3.1. Characterisation of catalysts

3.1.1. Surface morphology analysis

The morphology of the catalysts was investigated, and it can be seen from Fig. 1 that the Ni doping resulted in an obvious difference. From Fig. 1a, the surface of α-Fe₂O₃ presented irregular granular and needle-like structures. From Fig. 1b-e, after Ni doping, the surface showed an evenly distributed rice-like granular structure, and it gradually consolidated as the doping dosages above 10% (the best performance). Additionally, the EDS mapping showed that Fe, O and Ni were uniformly

dispersed on the surface of α-Ni₀.₂Fe₁.₈O₃, and the atomic ratio of Ni/Fe was 0.03 (Fig. 1f-i). While it was 0.095 (near the planned value of 0.1) after the digestion of α-Ni₀.₂Fe₁.₈O₃ via ICP measurement, indicating that the Ni^{2+} substituting Fe^{3+} mainly occurred inside the structure. From Fig. 1i, the atomic ratio of O/metal was 1.1 on the surface of α-Ni₀.₂Fe₁.₈O₃, and it was less than 1.5 on that of α-Fe₂O₃, suggesting the lack of O and inferring the formation of OVs.

From Fig. 1j-n, the TEM images showed that doping of Ni^{2+} obtained a more stable structure of α-Ni₀.₂Fe₁.₈O₃, and the particle size of it was evenly distributed at around 166.3 ± 39.2 nm (Fig. 1n). The exposed crystal planes of α-Fe₂O₃ with a d-spacing of 0.370 nm (belonged to (012) plane) and 0.265 nm (belonged to (110) plane) slightly increased to 0.379 nm and 0.270 nm in that of α-Ni₀.₂Fe₁.₈O₃ (Fig. 1k and m), respectively. It may be caused by the formation of Ni-O after Ni^{2+} substitution, which varied the length of Fe-O.

3.1.2. Crystal structure analysis

The crystal structures of the as-prepared catalysts were identified and compared with the standard XRD pattern of α-Fe₂O₃. From Fig. 2a, the crystal structures of as-synthesized materials with different Ni/Fe molar ratios were well-fitted to the standard α-Fe₂O₃ structure (PDF# 33–0664). The distinctive diffraction peaks at 24.2°, 33.2°, 35.7°, 40.9°, 49.5°, 54.1°, 62.4° and 64.0° could be assigned to the crystal plane of (012), (104), (110), (113), (024), (116), (214) and (300), respectively. Besides, there were no Ni-related peaks observed, indicating that Ni was successfully incorporated into the framework of α-Fe₂O₃, achieving isomorphic substitution rather than being loaded on the surface or forming Ni oxide. Additionally, the intensity of the diffraction peaks gradually decreased when the Ni doping ratio exceeded 10%, indicating a decrease in crystal structure strength, which might affect the catalytic performance. And the position of the peaks belonging to (110) and (104) planes marginally deviated to a lower angle (as shown in Fig S1). Based on Bragg's law, d($h k l$) = nλ/2sinθ, when the λ (X-ray wavelength) was fixed, the decrease of 2θ resulted in the increase of d($h k l$), which presented the interplanar crystal spacing. These results also matched with
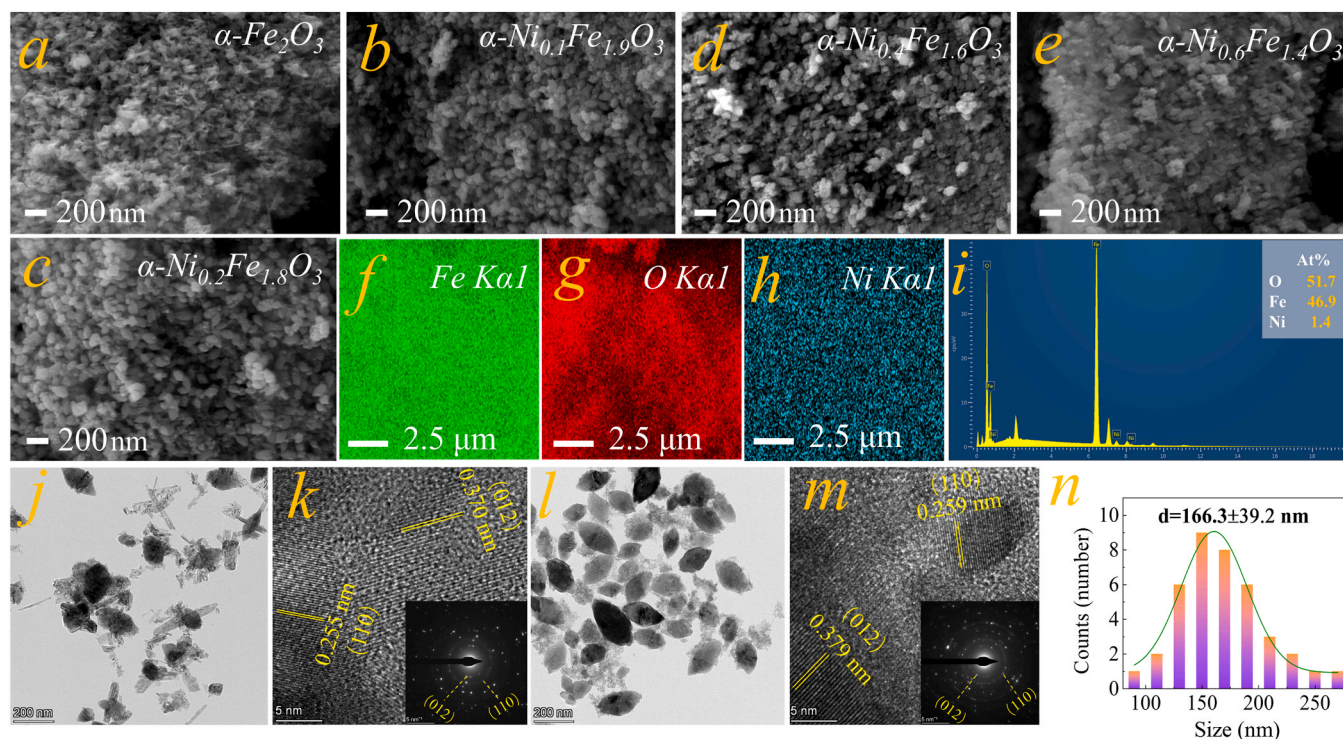
Fig. 1. SEM images of the as-synthesized catalysts (a-e); EDS analysis of α-Ni₀.₂Fe₁.₈O₃: mapping images of Fe, Ni, and O (f-h), energy spectrum image (i); HRTEM images: α-Fe₂O₃ (j), and α-Ni₀.₂Fe₁.₈O₃ (l); texture structures and cell diffraction: α-Fe₂O₃ (k), and α-Ni₀.₂Fe₁.₈O₃ (m); particle size distribution of α-Ni₀.₂Fe₁.₈O₃ (n).
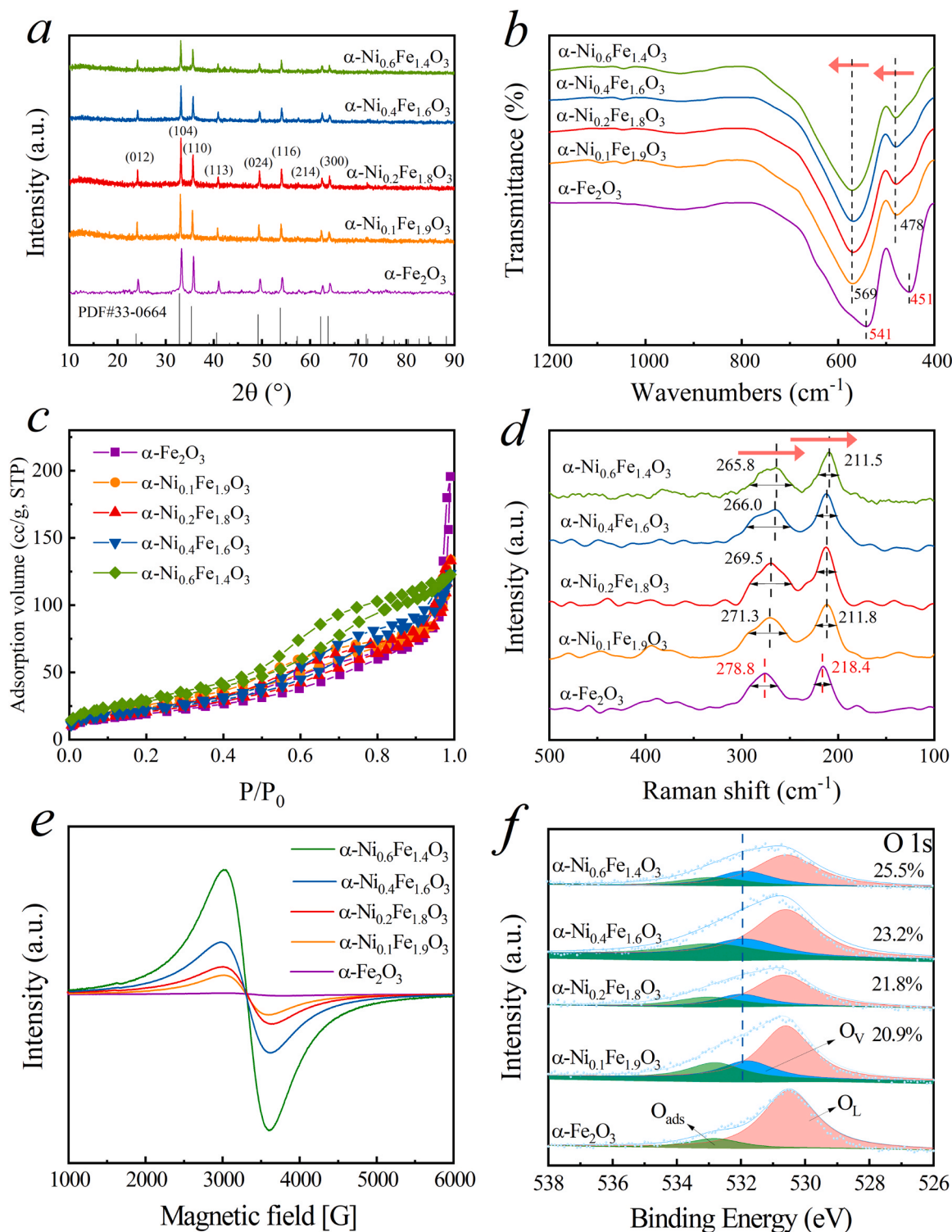
Fig. 2. Characterization of the catalysts. XRD patterns (a), FTIR spectra (b), N_2 adsorption-desorption isotherms (c), Raman spectra (d), ESR spectra (e), O 1s XPS spectra (f) of the catalysts.

the increased d-spacing of the (110) plane in TEM (Fig. 1k and m). This phenomenon may be induced by the altering of van der Waals forces in the structure of α-Fe_2O_3 after Ni^{2+} doping [36].

3.1.3. Surface functional groups analysis

The crystallinity of the catalysts decreased after Ni doping, thus the changing of the surface properties was analyzed by FTIR spectra. As Fig. 2b shows, the characteristic peaks at 451 and 541 cm^{-1} were

assigned to Fe-O of α-Fe_2O_3 [27]. Interestingly, with the insertion of Ni, these two peaks shifted to 478 and 569 cm^{-1}, indicating the formation of the Ni-O-Fe bond [27]. Furthermore, the intensity of the peak at 541 cm^{-1} was significantly reduced as the doped content, which might be due to the changed electronic structure of α-Fe_2O_3 caused by Ni^{2+} insertion, thus lengthening the Fe-O bond [36].

3.1.4. Specific surface area and pore size distribution analysis

The surface properties of the catalysts varied as Ni^{2+} doping. Meantime, the interior structure was also changed according to the N_2 adsorption-desorption processes. From Fig. 2c, compared with α-Fe_2O_3, the doped catalysts showed a relatively lower total pore volume as Ni^{2+}/ Fe^{3+} molar ratio increased. But the highest specific surface area (106 m^2/g) and average pore size (10.60 nm) were obtained by α-$Ni_{0.2}Fe_{1.8}O_3$, then decreased in α-$Ni_{0.4}Fe_{1.6}O_3$ and α-$Ni_{0.6}Fe_{1.4}O_3$ (Table S2). And the specific surface area enlarged 1.4 times of α-$Ni_{0.2}Fe_{1.8}O_3$ compared to α-Fe_2O_3 (72 m^2/g). The results were consistent with the gradually blocky surface as Ni^{2+} doping after aggregation (Fig. 1), which blocked the pore structure. The smaller specific surface area and consolidated surface morphology of α-$Ni_{0.4}Fe_{1.6}O_3$ and α-$Ni_{0.6}Fe_{1.4}O_3$ meant fewer metal sites exposed on the surface, which was not conducive to interaction with PMS.

3.1.5. OVs analysis

Due to the different charges and ionic radius between Ni^{2+} and Fe^{3+}, the charge balance and lattice distortion in the doping process jointly induced the lack of O in the structure of as-synthesized catalysts and changed their properties. Therefore, the OVs formed in the structure were declared in detail. As shown in TEM (Figs. 1k and 1m) and XRD spectra (Fig S1), Ni^{2+} doping in α-Fe_2O_3 caused the increase of crystal plane spacing, which led to the change of atomic spacing representing
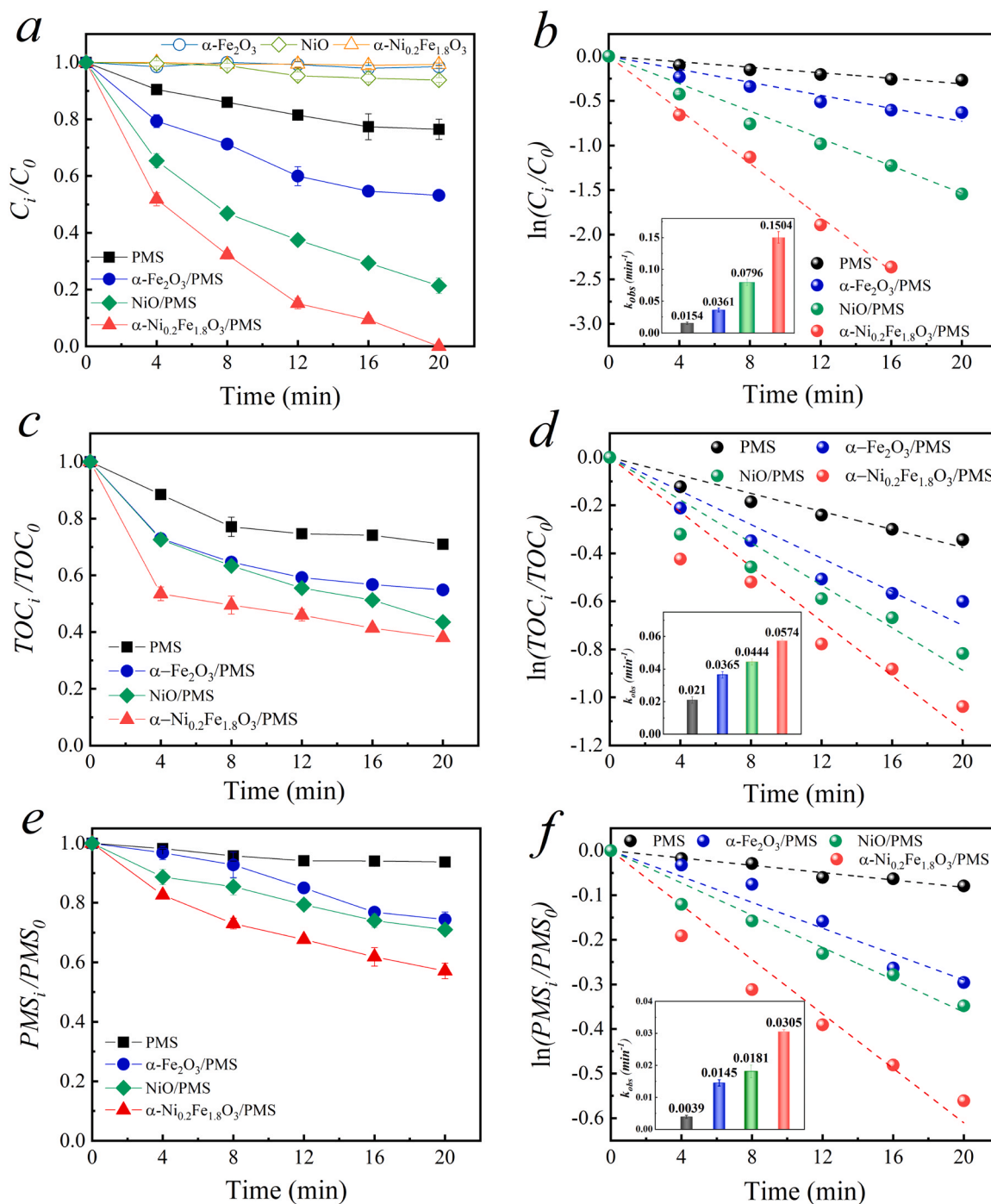
Fig. 3. Degradation (a, b) and mineralization rates (c, d) of aceclofenac, and decomposition of PMS (e, f) in different systems. Condition: $[ACF]_0 = 1.0$ mg/L, catalyst dose $= 100$ mg/L, $[PMS]_0 = 20$ mg/L, pH $= 7.0$, T $= 23$ °C.

the lattice distortion. Raman scattering is an effective method to detect defects and lattice disorders in crystals' structures [37]. As shown in Fig. 2d, the distinctive peaks at 218.4 cm^{-1}(Ag) and 278.8 cm^{-1}(Eg) fitted well in the typical Raman mode of α-Fe$_2$O$_3$ [22]. However, as the proportion of Ni doping increased, these two peaks gradually blue-shifted to 211.5 cm^{-1} and 265.8 cm^{-1}, respectively. Obviously, the OVs induced by doping of Ni^{2+} inevitably led to charge redistribution and affected the local electron density and lattice vibration frequency, which caused the blue shift in Raman spectra [38]. Besides, the full width at half maximum (FWHM) of the peak at 278.8 cm^{-1} increased from 29.3 cm^{-1} to 40.4, 41.6, 44.7 and 44.8 cm^{-1}, and the FWHM of the peak at 218.4 cm^{-1} also increased from 16.4 cm^{-1} to 20.9, 21.4, 21.8 and 22.1 cm^{-1} with the increase of Ni doping content. The asymmetrical broadening of the Raman line shape was caused by OVs in the crystal, which changed the mode correlation functions of the crystal [38,39]. The formation of OVs was also revealed via ESR spectra. From Fig. 2e, there was no signal observed of α-Fe$_2$O$_3$. However, a significant signal at g= 2.003 belonged to the unpaired electrons of OVs that appeared in the as-synthesized catalysts with Ni^{2+} doping [40], and the intensity of the signal enhanced gradually, indicating that more OVs were formed. The content of OVs was quantified via the deconvolution XPS spectra of O 1s. From Fig. 2f, the binding energies at 530.6, 531.9 and 532.8 eV ascribed to the lattice oxygen (O$_L$), low-coordinated oxygen adsorbed in OVs (O$_V$), surface-chemisorbed oxygen (O$_{ads}$) [41], respectively. The relative content of O$_V$ gradually increased with Ni^{2+} doping, indicating that doping of Ni^{2+} could effectively construct OVs in the structure of α-Fe$_2$O$_3$.

3.2. Evaluation of catalytic performance

The catalytic performance of the catalysts was evaluated by ACF removal and compared with α-Fe$_2$O$_3$. From Fig. 3a, ACF was barely removed by α-Fe$_2$O$_3$, NiO and α-Ni$_{0.2}$Fe$_{1.8}$O$_3$. Additionally, the changing of Ni^{2+} doping dosage in catalysts had no effect on their adsorption capacity for ACF removal (Fig S2). For PMS oxidation alone, just 24.0% of ACF was removed. While the degradation efficiency of ACF increased to 47.0%, 88.6% and 100% with the presence of α-Fe$_2$O$_3$, NiO and α-Ni$_{0.2}$Fe$_{1.8}$O$_3$, respectively. Meantime, the apparent reaction rate constant (k_{obs}) of ACF degradation enhanced greatly from 0.015 min^{-1} of the sole PMS to 0.036 min^{-1} and 0.079 min^{-1} of the α-Fe$_2$O$_3$/PMS and NiO/PMS process, respectively. And the k_{obs} value was enhanced 10 times in the α-Ni$_{0.2}$Fe$_{1.8}$O$_3$/PMS system compared to PMS alone, illustrating the high catalytic efficiency of α-Ni$_{0.2}$Fe$_{1.8}$O$_3$ (Fig. 3b). Besides, α-Ni$_{0.2}$Fe$_{1.8}$O$_3$ presented lower leaching of iron ion (3 μg/L) and nickel ion (7 μg/L) than that of α-Fe$_2$O$_3$ (6 μg/L) and NiO (25 μg/L, beyond 20 μg /L limited by EU), respectively. It also showed the highest removal rate and the k_{obs} value for ACF degradation than those catalysts with different Ni^{2+}/Fe^{3+} ratios (Fig S2).

The performance of α-Ni$_{0.2}$Fe$_{1.8}$O$_3$ for PMS activation was also evaluated by the mineralization process of ACF. As presented in Fig. 3c, during the α-Ni$_{0.2}$Fe$_{1.8}$O$_3$ activated process, the mineralization rate of ACF increased by 32.0%, 16.0% and 6.0% compared with the sole PMS, α-Fe$_2$O$_3$/PMS and NiO/PMS systems, respectively. Moreover, the highest k_{obs} of the mineralization process were also reached by α-Ni$_{0.2}$Fe$_{1.8}$O$_3$/PMS system, which was 3 times that of the PMS alone process (Fig. 3d).

The α-Ni$_{0.2}$Fe$_{1.8}$O$_3$ activated process showed high performance for ACF degradation and mineralization than PMS alone. Therefore, the decomposition of PMS during the activation process was also evaluated. From Fig. 3e-f, the self-decomposition rate of PMS was slow, indicating less PMS reacted with ACF in the sole PMS process and induced a relatively low removal rate of it. The presence of α-Fe$_2$O$_3$, NiO and α-Ni$_{0.2}$Fe$_{1.8}$O$_3$ caused the quick decomposition of PMS, especially in the α-Ni$_{0.2}$Fe$_{1.8}$O$_3$/PMS system, which was 7.8, 2.1 and 1.7 times that of PMS alone, α-Fe$_2$O$_3$/PMS and NiO/PMS process, respectively. Based on the high removal rates, the acceleration of PMS decomposition might

induce the generation of ROS and greatly contribute to ACF degradation.

3.3. Effect of various water matrix factors

3.3.1. Solution pH

Considering that the solution pH has a great influence on the existing form of PMS (pKa$_1$ <0, pKa$_2$ =9.4) and ACF (pKa=4.7), and the surface charge of the catalyst [42], a wide pH range of 3.0–11.0 was investigated. From Fig. 4a and Fig S3a, neither acid nor base conditions benefited the activation process. And α-Ni$_{0.2}$Fe$_{1.8}$O$_3$ showed high efficiency for PMS activation at around neutral conditions. This may be induced by the different reaction mechanisms of PMS and ACF on the catalyst's surface as the solution pH altered. The protonated surface of the catalyst was positively charged at pH below the pHpzc of α-Ni$_{0.2}$Fe$_{1.8}$O$_3$ (6.8), which also hardly contacted with ACF mainly as the molecular form in this case. Besides, the PMS was more stable and harder to activate in acidic conditions. These factors combined to cause the poor removal rate of ACF by the catalytic system. When the pH exceeded the pH$_{pzc}$ (6.8) of α-Ni$_{0.2}$Fe$_{1.8}$O$_3$, the deprotonation process induced a negative charge surface of it, thus hindering the interface process due to electrostatic repulsion of PMS and ACF (pKa=4.7) in the form of negative ions. On the contrary, the degradation of ACF by alone PMS under different pH presented a different trend that gradually accelerated with the increasing pH and significantly enhanced at pH= 11 (Fig S3b). This process may be induced by PMS activation under basic conditions, thus promoting the generation of ROS [43]. Nevertheless, the α-Ni$_{0.2}$Fe$_{1.8}$O$_3$ activated process showed better performance and higher reaction rate compared to the PMS alone in each pH value.

3.3.2. Reaction temperature

The reaction temperature critically affected the amount of activated PMS molecules and supplied energy for the interface process [44]. Herein, it was considered during the degradation of ACF. From Fig. 4b and Fig S4, increasing reaction temperature mediated a significant acceleration of ACF degradation. The activation energy (Ea, kJ mol^{-1}) of the α-Ni$_{0.2}$Fe$_{1.8}$O$_3$/PMS system was calculated via lnk_{obs}=lnA-Ea/RT. Where k_{obs} is the pseudo-first-order kinetic rate constant, A is the pre-exponential factor or Arrhenius constant, and R is the gas constant (8.314 J•mol^{-1} K^{-1}). From Fig. 4c and Fig S4, the T^{-1} and lnk_{obs} of α-Fe$_2$O$_3$/PMS/ACF and α-Ni$_{0.2}$Fe$_{1.8}$O$_3$/PMS/ACF system presented a good linear relationship. The Ea was 34.4 kJ/mol by α-Fe$_2$O$_3$ activated process and noticeably decreased to 21.0 kJ/mol that by α-Ni$_{0.2}$Fe$_{1.8}$O$_3$, indicating Ni doping notably improved the catalytic performance of α-Fe$_2$O$_3$ and reduced the activation energy. Moreover, the Ea value (21.0 kJ/mol) was still higher than that of diffusion-controlled reactions (10–13 kJ/mol), suggesting that the removal of ACF was dominated by the chemical reaction rate on the surface of α-Ni$_{0.2}$Fe$_{1.8}$O$_3$ rather than absorption rate [45].

3.3.3. Catalyst stability investigation

The reuse ability of α-Ni$_{0.2}$Fe$_{1.8}$O$_3$ was evaluated by several cycles to activate PMS for ACF degradation. From Fig. 4d, the degradation efficiency of ACF by α-Ni$_{0.2}$Fe$_{1.8}$O$_3$/PMS system was above 97% in three cycles, and it was still more than 82% after five cycles. Additionally, the k_{obs} value slightly changed in three cycles, while it decreased gradually with use times in the α-Fe$_2$O$_3$/PMS system (Fig S5a). The crystal structure of α-Ni$_{0.2}$Fe$_{1.8}$O$_3$ and α-Fe$_2$O$_3$ both showed no obvious change, which were demonstrated by the XRD spectra after use (Fig S5b). However, the leaching of iron ions was below 3 μg/L during the cycle of α-Ni$_{0.2}$Fe$_{1.8}$O$_3$ and far less than that of α-Fe$_2$O$_3$ (Fig S5c), illustrating α-Ni$_{0.2}$Fe$_{1.8}$O$_3$ was stabler after Ni^{2+} doping. Meantime, the leaching of nickel ions as shown in Fig S5d was less than 7 μg/L in five runs (far less than 20 μg /L limited by EU).

3.3.4. Performance of α-Ni$_{0.2}$Fe$_{1.8}$O$_3$ in actual water

The performance of α-Ni$_{0.2}$Fe$_{1.8}$O$_3$ for PMS activation was evaluated
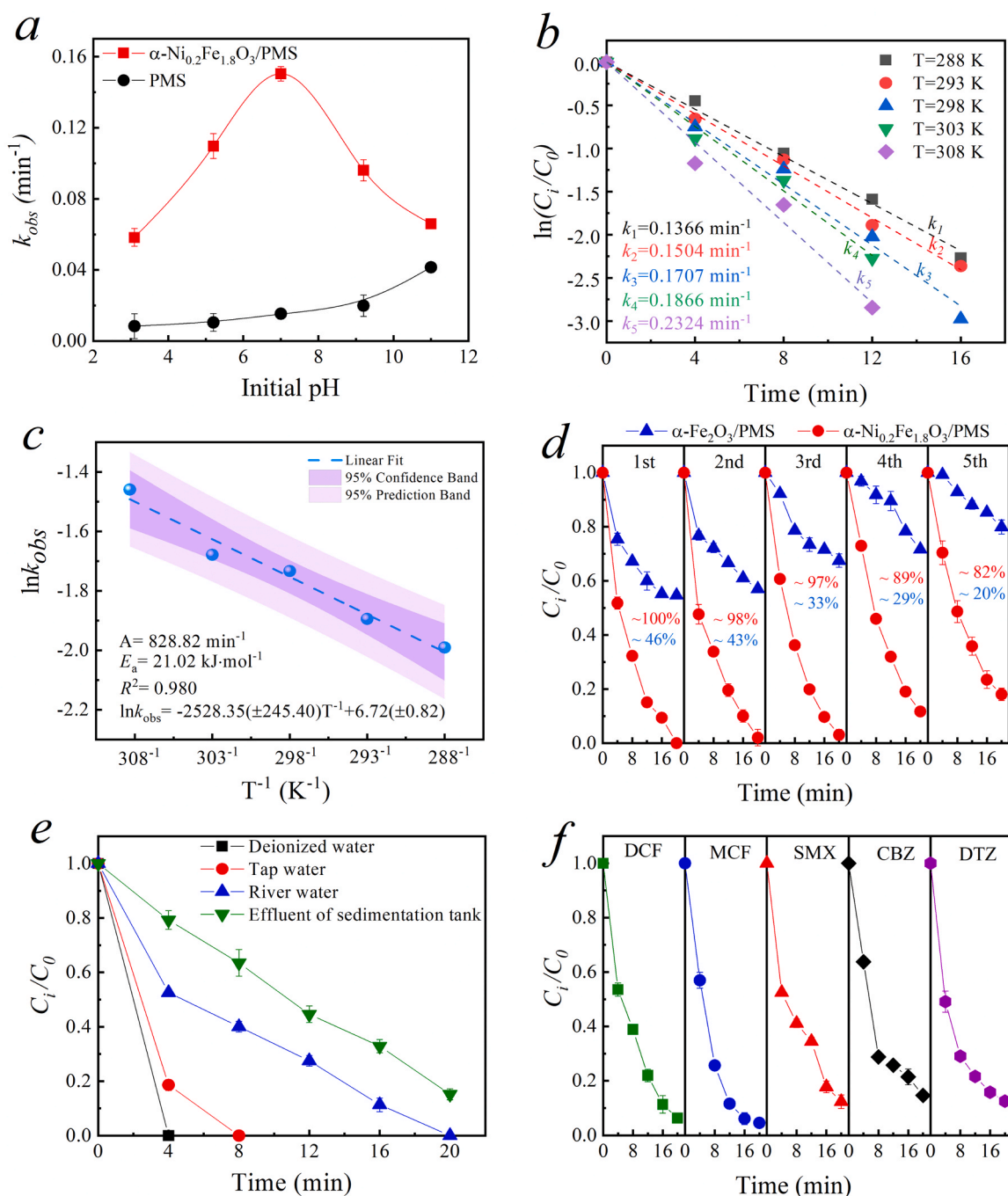
Fig. 4. Effect of different pH (a) and temperature (b, c) on the degradation of ACF by α-Ni$_{0.2}$Fe$_{1.8}$O$_3$/PMS system. Cycling experiments of α-Fe$_2$O$_3$ and α-Ni$_{0.2}$Fe$_{1.8}$O$_3$ activating PMS for the degradation of ACF (d), degradation of ACF in natural water samples by α-Ni$_{0.2}$Fe$_{1.8}$O$_3$/PMS system (e), degradation of DCF, MCF, SMX, CBZ and DTZ by α-Ni$_{0.2}$Fe$_{1.8}$O$_3$/PMS system (f). Condition: [Pollutions]$_0$ = 1 mg/L (100 μg/L for actual water), catalyst dose = 100 mg/L, [PMS]$_0$ = 20 mg/L, pH = 7.0, T = 23 °C. (T = 15, 20, 25, 30, 35 °C for (b)).

in different water samples. The water quality parameters of deionized water (DW), tap water (TW), river water (RW), and effluent of the sedimentation tank in the wastewater treatment plant (SW) are shown in Table S3. From Fig. 4e, ACF could be rapidly removed in the DW and TW within 4 min and 8 min, respectively, and thoroughly removed within 20 min in RW. Even though the TOC of SW was higher at 8.6 mgC/L, the removal rate of ACF still reached 82%. Overall, the degradation rate of ACF in different water were negatively related to their content of TOC. The α-Ni$_{0.2}$Fe$_{1.8}$O$_3$/PMS system was also employed for degrading a series of pharmaceutical and personal care products (PPCPs). The DCF, MCF, SMX and CBZ are all commonly used drugs for anti-inflammatory

and analgesic purposes, and DTZ is widely used to enhance the image of organs during diagnostic detection, which are all frequently detected in the surface water and threaten the ecological environment [46,47]. From Fig. 4f, more than 95% of DCF and MCF could be degraded within 20 min. The removal rate reached 85% for SMX, CBZ and DTZ degradation. These results comprehensively demonstrated the high performance of α-Ni$_{0.2}$Fe$_{1.8}$O$_3$ during application.

3.4. ROS investigation

3.4.1. Identification of ROS

To unveil the potential ROS generated in the α-Ni$_{0.2}$Fe$_{1.8}$O$_3$/PMS system, ESR tests with spin-trapping agents (DMPO and TEMP) were conducted and the signal was monitored at specific time intervals. As shown in Fig. 5a-b, the distinguishing characteristic peaks of DMPO-

$\bullet$OH (the intensity of 1:2:2:1), DMPO-SO$_4^{\bullet-}$ (the weak peaks accompanied DMPO-$\bullet$OH) and DMPO-O$_2^{\bullet-}$ were detected in α-Ni$_{0.2}$Fe$_{1.8}$O$_3$/PMS system, which was unable to observe in the PMS alone system [48]. Additionally, these signal intensities were markedly enhanced compared to α-Fe$_2$O$_3$/PMS process (Fig. S6a-b), illustrating that a larger amount of these radicals generated by α-Ni$_{0.2}$Fe$_{1.8}$O$_3$ activated PMS.

Interestingly, the intensity of the peak assigned to DMPO-$\bullet$OH and
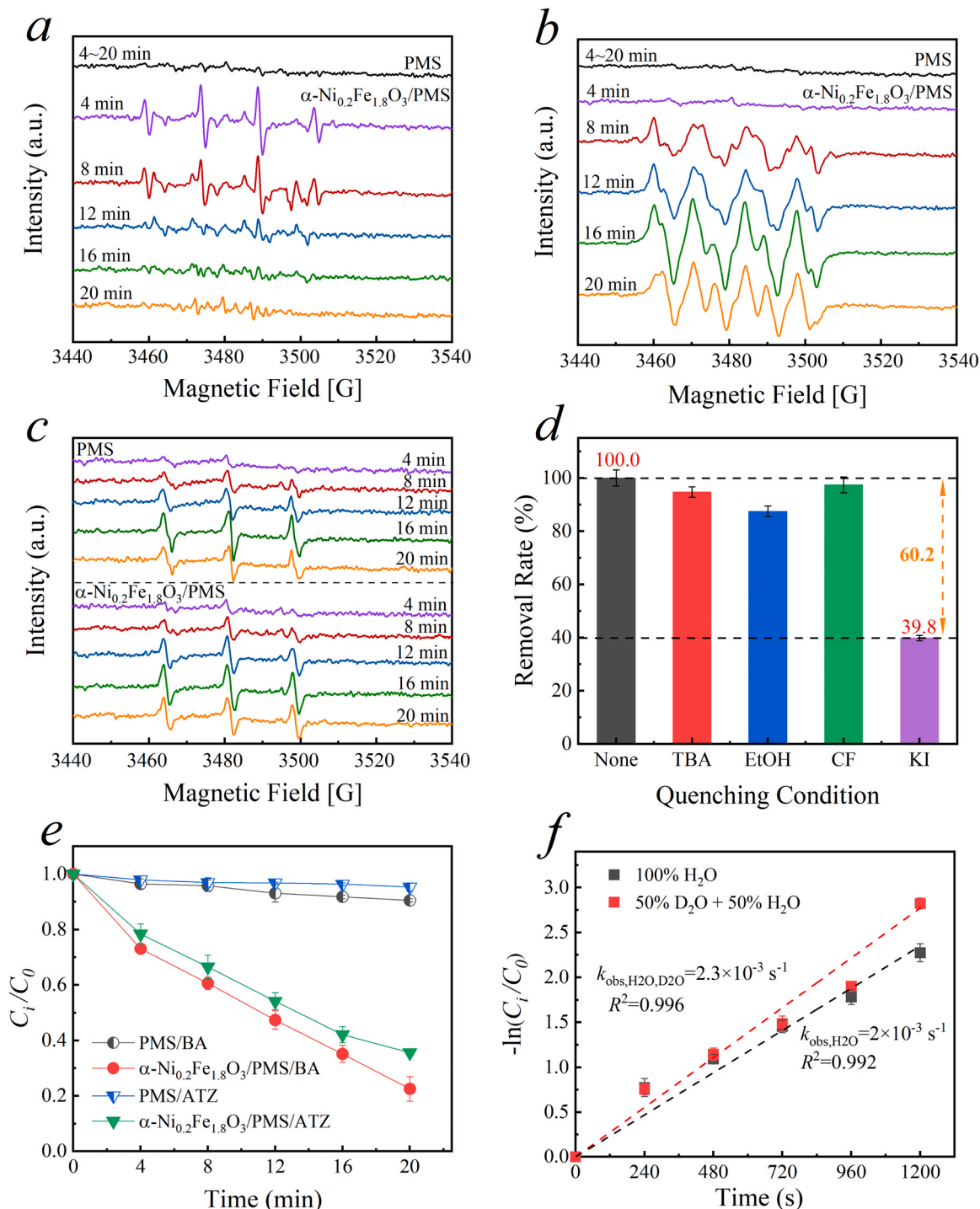
Fig. 5. DMPO spin-trapping ESR spectra of DMPO-OH, DMPO-SO$_4$ (a) and DMPO-O$_2$ (b); TEMP spin-trapping ESR spectra of TEMPO (c) in PMS alone and α-Ni$_{0.2}$Fe$_{1.8}$O$_3$/PMS system. Effect of TBA, EtOH, KI and CF on the degradation of ACF (d), degradation of ATZ and BA by α-Ni$_{0.2}$Fe$_{1.8}$O$_3$/PMS system (e); degradation of ACF by α-Ni$_{0.2}$Fe$_{1.8}$O$_3$/PMS system in H$_2$O and D$_2$O (f). Condition: [ACF]$_0$ = 1.0 mg/L, [ATZ]$_0$ = [BA]$_0$ = 0.5 mg/L, [DMPO]$_0$ = 100 mmol/L, [TEMP]$_0$ = 50 mmol/L, catalyst dose = 100 mg/L, [PMS]$_0$ = 20 mg/L = 0.065 mmol/L, [TBA]$_0$ = [EtOH]$_0$ = [CF]$_0$ = 6.5 mmol/L, [KI]$_0$ = 0.65 mmol/L, pH = 7.0, T = 23 °C.

DMPO-$SO_4^{\bullet-}$ reached the highest at 4 min, then gradually decayed. Meantime, the intensity of the peak belonged to DMPO-$O_2^{\bullet-}$ gradually increased in 0–16 min and then declined (Fig. 5b). The phenomenon indicated that $SO_4^{\bullet-}$ and •OH were mainly generated in 0–4 min and then self-quenched or converted to other active species. It was noteworthy that the generated $SO_4^{\bullet-}$ and •OH in the first 4 min caused 48% of ACF to degrade, indicating the crucial role of them.

Unlike $SO_4^{\bullet-}$, •OH and $O_2^{\bullet-}$, the characteristic 1:1:1 triplet belonged to $^1O_2$ were all detected in the alone PMS, α-Fe_2O_3/PMS and α-$Ni_{0.2}Fe_{1.8}O_3$/PMS systems. However, the intensity of the signal showed almost no difference among these systems (Fig. S6c). From Fig. 5c, the intensity of the signal was almost not changed with time in the PMS alone and α-$Ni_{0.2}Fe_{1.8}O_3$/PMS systems. Interestingly, through a first-order linear fitting, the results in Fig S7 indicated that the increase rate of TEMPO in the PMS alone system (k_1=29179.88 min^{-1}) was even higher than that of α-$Ni_{0.2}Fe_{1.8}O_3$/PMS system (k_2=26508.78 min^{-1}), revealing that the $^1O_2$ mainly generated by self-decomposition rather than the activated process of PMS. Considering the low removal rate of ACF by PMS alone, inferring that $^1O_2$ barely contributed to the degradation of ACF.

3.4.2. Contribution of ROS

The roles of the detected ROS during ACF degradation were evaluated by quenching tests. Due to the rapid reaction with •OH ($k =$ (3.8 −7.6) × 10^8 M^{-1} s^{-1}) and low rapid reaction towards $SO_4^{\bullet-}$ ($k =$ (4.0–9.1) × 10^5 M^{-1} s^{-1}), TBA is universally used as the scavenger for •OH [49]. In contrast, EtOH can quickly react with both $SO_4^{\bullet-}$ ($k = 2.5 \times 10^7$ M^{-1} s^{-1}) and •OH ($k = 9.7 \times 10^8$ M^{-1} s^{-1}) [50]. Therefore, they were preliminarily employed to estimate the contribution of $SO_4^{\bullet-}$ and •OH. The reaction rate between CF and $O_2^{\bullet-}$ is 2.3×10^8 M^{-1} s^{-1}, which is much higher than that of •OH ($k = 5.4 \times 10^7$ M^{-1} s^{-1}) and $^1O_2$ (barely react) [51]. Meantime, due to the low octanol-water portion coefficient (1.97), CF is suitable to quench the surface-bonded $O_2^{\bullet-}$ in a multiradical system [52].

From Fig. 5d, the TBA and EtOH at a molar concentration of 100 times that of PMS showed slight inhibition on ACF degradation, which was only 5.3% and 12.5%, respectively. Moreover, the removal of ACF was still slightly inhibited with a sufficient concentration of them (500 times that of PMS) as shown in Fig S8a. This phenomenon was not well in line with the results obtained via ESR spectra that $SO_4^{\bullet-}$ and •OH played a crucial role. ATZ and BA as typical probe compounds for $SO_4^{\bullet-}$ and •OH have been evidenced to rarely react with $O_2^{\bullet-}$ and $^1O_2$, and thus were employed for further investigation [53].

From Fig. 5e, the degradation efficiency of ATZ and BA by α-$Ni_{0.2}Fe_{1.8}O_3$/PMS system achieved 62.0% and 80.0%, respectively, indicating that the $SO_4^{\bullet-}$ and •OH were crucial radicals attributed to the system. In previous studies, surface-bond radicals were always the reason for slight inhibition of TBA and EtOH, which are both hydrophilic scavengers that hardly accumulate on the catalyst surface [54]. Moreover, KI was widely used to distinguish the surface-bonded $SO_{4,ads}^{\bullet-}$ and $\bullet OH_{ads}$ [55]. Herein, a relatively low concentration of KI (10 times that of PMS) was added to reduce the direct reaction between I^- and PMS. From Fig. 5d, the removal rate of ACF decreased by 60.2% after KI was added. Additionally, the decomposition of PMS was slightly affected by KI (Fig. S9), illustrating the decrease of ACF degradation was caused by the quenching of $SO_{4,ads}^{\bullet-}$ and $\bullet OH_{ads}$.

The addition of CF as 100 times of PMS just showed negligible inhibition of ACF degradation (Fig. 5d). Even the CF concentration increased to 500 times of PMS, the degradation of ACF only decreased by 10% (Fig. S8b), indicating that the $O_2^{\bullet-}$ was not the dominant ROS in the α-$Ni_{0.2}Fe_{1.8}O_3$/PMS system. Based on the longer lifetime of $^1O_2$ in D_2O than H_2O, the kinetic solvent isotope effect (KSIE) was used to examine the contribution of $^1O_2$ in the mixture of D_2O and H_2O (v/v: 50/50) [56]. From Fig. 5f, the k_{obs} of ACF degradation only slightly increased in the mixed solution ($k_{obs,H_2O,D_2O} = 2.3 \times 10^{-3} s^{-1}$ vs $k_{obs,H_2O} = 2.0 \times 10^{-3} s^{-1}$).

The reaction rate constant between $^1O_2$ and ACF in H_2O was calculated to be $2.27 \times 10^{-4} s^{-1}$ according to Eq. 1, thus the quantized contribution of $^1O_2$ for ACF degradation was 11.4% according to Eq. 2 (details in Text S6).

$$k_{1_{O_2,H_2O}} = \frac{k_{obs,H_2O,D_2O} - k_{obs,H_2O}}{\frac{k_{H_2O}}{x_{H_2O} \cdot k_{H_2O} + x_{D_2O} \cdot k_{D_2O}} - 1} \tag{1}$$

$$contribution rate (\%) = k_{1_{O_2,H_2O}} \Big/ k_{obs,H_2O} \times 100\% \tag{2}$$

In conclusion, $O_2^{\bullet-}$ and $^1O_2$ made little contribution to the degradation of ACF, while surface-bond $SO_4^{\bullet-}$ and •OH played the dominant role.

3.5. Interface mechanism of ROS generation

#### 3.5.1. Interface process investigation

Doping of Ni^{2+} in α-$Ni_{0.2}Fe_{1.8}O_3$ may improve the electron transfer in the structure, thus benefitting the activation of PMS [27]. From Fig. 6a, the CV curve and EIS image of α-$Ni_{0.2}Fe_{1.8}O_3$ showed a higher current density and lower charge transfer resistance value than that of α-Fe_2O_3, meaning it was more conducive to electron transfer. The open-circuit potential curves of glassy carbon electrode (GCE) coated α-$Ni_{0.2}Fe_{1.8}O_3$ after adding PMS or ACF were monitored to declare the electron transfer process. From Fig. 6b, compared with α-Fe_2O_3, the open-circuit potential by α-$Ni_{0.2}Fe_{1.8}O_3$ significantly increased after PMS injection, and it was positively correlated with PMS concentration (Fig S10), demonstrating that the electron transfer from α-$Ni_{0.2}Fe_{1.8}O_3$ to PMS, and more PMS could facilitate this process. Different from previous studies [44], the addition of ACF with a high concentration (1 M) didn't induce a remarkable drop of the potential, revealing that the mechanism of ACF donating electrons to metastable reaction complexes could be excluded in these two systems [57], and the increasing potential of catalyst surface mainly derived from the formation of reactive surface-bond radicals.

The transmission coefficient (α) as a credible parameter to evaluate the electron transfer mechanism [44,58], was calculated according to Eq. 3 in α-$Ni_{0.2}Fe_{1.8}O_3$/PMS system. And four phenolic compounds (the standard electrode potential (E^0) of PE, 4-CP, BPA, 2,4-DCP was 1.003, 0.945, 0.917 and 0.909 V, respectively) were selected as target one-electron transfer compounds to establish quantitative structure–activity relationships (QSAR) of α-$Ni_{0.2}Fe_{1.8}O_3$/PMS system. Generally, α ≈ 1 means the electron transfer rate plays the dominant role, and α < 0.5 indicates that the mass transfer between two substances in contact is the rate-limiting step in the process [44]. From Fig. 6c-d, the E^0 and logk_{obs} of four PCs presented an excellent linear relationship, and the α value was calculated as 0.15 ± 0.03, illustrating the electron transfer process critically relied on the mass transfer from PMS to the α-$Ni_{0.2}Fe_{1.8}O_3$. In other words, the surface-complex of PMS on α-$Ni_{0.2}Fe_{1.8}O_3$ is the crucial step dominating the electron transfer.

$$\log k_{obs} = -\alpha \frac{E^0}{0.059} + \beta \tag{3}$$

The presence of OVs could cause more exposed unsaturated metal sites on the catalyst surface, which may serve as Lewis acid sites (LASs) to adsorb and complex the water molecules and oxidants [59]. From Fig. 6e, the distinctive peaks at 1448, 1489 and 1608 cm^{-1} in α-Fe_2O_3 were assigned to the adsorption of pyridine on Lewis acid sites [29]. The intensity of these peaks obviously enhanced and the peak position slightly shifted to lower wavenumbers in α-$Ni_{0.2}Fe_{1.8}O_3$. The content of LASs on α-$Ni_{0.2}Fe_{1.8}O_3$ was 53.0 μmol/g, which was much higher than that of α-Fe_2O_3 (27.0 μmol/g), thus benefiting the surface complex process on the OVs.

The interface reaction between HSO_5^- and α-$Ni_{0.2}Fe_{1.8}O_3$ including the role of H_2O was explored by in situ ATR-FTIR and Raman processes. And the IR and Raman spectra of HSO_5^- and SO_4^{2-} in water were simulated in the Gaussian procedure to identify the vibrations of the structures
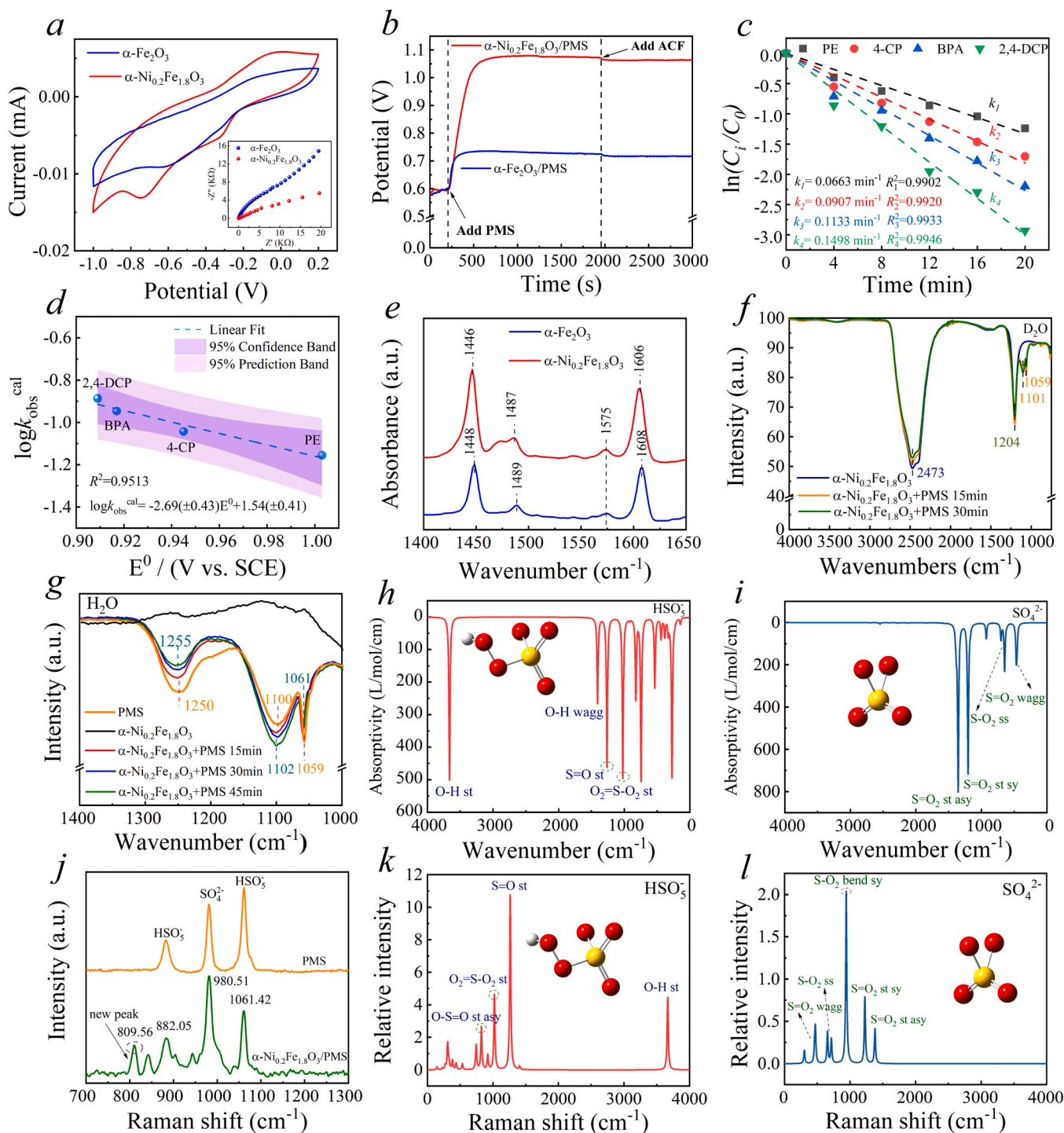
Fig. 6. Cyclic voltammetry and EIS Nyquist plots (a), open-circuit potential curves on the α-Fe$_2$O$_3$ and α-Ni$_{0.2}$Fe$_{1.8}$O$_3$ electrodes (b), degradation curves of different PCs (c) and correlation of chemical reaction kinetic parameters to their standard electrode potentials (d) by the α-Ni$_{0.2}$Fe$_{1.8}$O$_3$/PMS system, infrared spectra of adsorbed pyridine (e). In situ Raman and ATR-FTIR spectra of PMS alone and α-Ni$_{0.2}$Fe$_{1.8}$O$_3$/PMS system (f, g, j), computed anharmonic spectra for HSO$_5^-$ and SO$_4^{2-}$ of Raman and ATR spectra, obtained at the B3LYP/6–311 +G(2df,2p) level of theory (h, i, k, l), respectively. Condition: [PCs]$_0$ = 0.1 mM, catalyst dose = 100 mg/L, [PMS]$_0$ = 20 mg/L, pH = 7.0, T = 23 ℃.

(Table S4-S7) for the first time, which made the analysis in this study more credible and could provide reference for later study. From Fig. 6f, the combination of metal sites and water molecules during the interaction process was investigated in heavy water (D$_2$O) via ATR-FTIR spectra to minimize the influence of H$_2$O in the external environment. The peak at 2473 cm^{-1} was detected when α-Ni$_{0.2}$Fe$_{1.8}$O$_3$ was added, which was attributed to the Me-OD group [29], illustrating the

adsorption of surface -OD on the metal sites. Interestingly, after the addition of PMS, the intensity of it decreased gradually with time, indicating that part of the surface -OD was replaced by HSO$_5^-$ (Eq. 4).

From Fig. 6g of the ATR-FTIR spectra, three distinctive peaks at 1059, 1100 and 1250 cm^{-1} were observed in the PMS solution. Combined with the simulated spectra in Fig. 6h and Fig. 6i, the peaks at 1059 and 1250 cm^{-1} were attributed to HSO$_5^-$, and the peak at 1100 cm^{-1}

belonged to SO_4^{2-}. The intensity of peaks belonging to HSO_5^- significantly decreased after α-$Ni_{0.2}Fe_{1.8}O_3$ was added and gradually declined with time. Meantime, the peak ascribed to SO_4^{2-} increased, indicating HSO_5^- was finally conversed to SO_4^{2-}. The peak at 1057 cm^{-1} assigned to S-O(O) vibration of HSO_5^- shifted to 1061 cm^{-1} in the presence of α-$Ni_{0.2}Fe_{1.8}O_3$. This blue shift was caused by the strengthened S-O when the O-O of the $H-O-O-SO_3$ structure bonded to the surface of α-$Ni_{0.2}Fe_{1.8}O_3$. The surface-bonded O-O accepted the electron from the active metal sites and decreased the electron drawing from the neighboring S−O, thus making it stronger [42,57]. And this electron transfer via O-O of the surface-complexed HSO_5^- might make the O-O bond break and generate $SO_4^{\bullet-}$ (Eq. 5).

Combined with the results in Fig. 6j-l, the peaks at 882.05 and 1061.42 cm^{-1} in the in-situ Raman spectra attributed to HSO_5^- significantly decreased, and the peak at 980.51 cm^{-1} of SO_4^{2-} inversely enhanced after α-$Ni_{0.2}Fe_{1.8}O_3$ was added. Meanwhile, a new peak at 809.56 cm^{-1} appeared, which corresponded to the vibration of prolonged O−O bond of the surface-complexed metastable $Me-\bullet OOSO_3$, and this formed peroxo species was readily decomposed to generate $SO_4^{\bullet-}$ (Eqs. 6–7) [42,60].

$$\equiv Me^{n+} - {}^-OH + HSO_5^- \rightarrow \equiv Me^{n+} - (HO)OSO_3^- + OH^- \tag{4}$$

$$\equiv Me^{n+} - (HO)OSO_3^- \rightarrow \equiv Me^{(n+1)+} - {}^-OH + SO_4^{\cdot -} \tag{5}$$

$$\equiv Me^{(n+1)+} - {}^-OH + HSO_5^- \rightarrow \equiv Me^{n+} - {}^{\cdot}OOSO_3^- + H_2O \tag{6}$$

$$2 \equiv Me^{n+} - {}^{\cdot}OOSO_3^- + 2H_2O \rightarrow 2 \equiv Me^{n+} - {}^-OH + O_2 + 2SO_4^{\cdot -} + 2H^+ \tag{7}$$
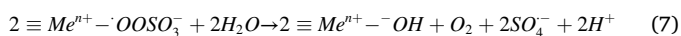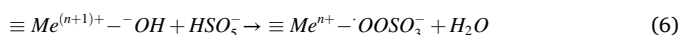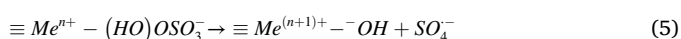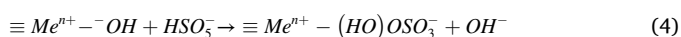
3.5.2. Revealing of interaction process by DFT study

Furthermore, the DFT study was carried out to reveal and prove the process of PMS replacing the surface -OH to surface-complex with metal sites and activated via OVs at a more microscopic level. The OVs readily serve as adsorption sites of O atoms (such as O of H_2O and HSO_5^-), contributing to the combination of adjacent metal sites with adsorbed O [61]. Considering the order of addition and the results of in-situ ATR-FTIR, the H_2O was believed to be preferentially in contact with OVs, which was highly susceptible to dissociation into hydroxyl groups [62]. From Fig. 7a, the OV structural model was constructed on the exposed (110) plane of α-$Ni_{0.2}Fe_{1.8}O_3$, which was observed by the HRTEM images and varied after Ni^{2+} doping in the XRD spectra. From Fig. S11~S12, the results illustrated the most stable structure for adsorbing H_2O on the (110) plane in α-Fe_2O_3 and α-$Ni_{0.2}Fe_{1.8}O_3$ were Fe-Fe and Ni-Fe 'bridge' modes, respectively. Another exposed plane of (012) in α-$Ni_{0.2}Fe_{1.8}O_3$ structure was also evidenced that has a lower adsorption ability of H_2O compared with (110) plane (Fig. S13). The process of adsorption and dissociation of H_2O and how HSO_5^- replaced the -OH to surface-complex with unsaturated metal sites around OVs was traced and elucidated by Gibbs free energies (ΔG) profiles in Fig. 7b. Wherein, RC represented for reactant, PC represented for product, IM represented for intermediate and TS represented for transition state. The H_2O firstly adsorbed on unsaturated Ni and Fe sites around OVs by bridge mode with the adsorption energy (E_{ads}) of − 1.66 eV, then dissociated into hydroxyl group and the detached H atom adsorbed on the surrounding O atom, the ΔG (−1.45 eV) of which indicated the spontaneity of the reaction.

Before introducing HSO_5^- into the reaction system, the bonding sites (O_I or O_{II}) of $H-O_I-O_{II}-SO_{III3}^-$ with metal sites were priorly discussed, which would differently lead to the generation of $SO_4^{\bullet-}$ and $\bullet OH$ (Fig. 7c_I-c_{II}) due to the cleavage of O_I-O_{II} bond, respectively. As shown in Fig. 7c_{III} and Fig. 7c_{IV}, the bond length of Fe-O_I (2.017 Å) and Ni-O_I (2.021 Å) was shorter than that of Fe-O_{II} (2.197 Å) and Ni-O_{II} (2.240 Å). Meantime, the E_{ads} of HSO_5^- with O_I bonded to metal sites (−7.72 eV) on the catalyst surface was lower than that of O_{II} (−4.34 eV), indicating HSO_5^- was more readily bonded with metal sites through O_I to maintain a stable structure, and thus generating $SO_4^{\bullet-}$.

As shown in Fig. 7b, when introducing $H-O_I-O_{II}-SO_{III3}^-$ near OV already occupied by -OH group (RC2), it was stepwisely absorbed on the surface through O_{III} bonding with two unsaturated Fe sites around OV (IM2-IM3). And in that adsorption process, the $H-O_I-O_{II}-$ of HSO_5^- gradually approached the OV center, while the surface -OH group incrementally side-shifted away OV at the same time, which tended to undergo ligand exchange reaction. In the excited state (TS1), the -OH group has completely moved from the position occupying the OV center to the side. And low energy barrier (ΔE_1) of 0.73 eV from IM3 to TS1 meant the ligand exchange reaction was easy to occur. After that, the HSO_5^- was completely absorbed on OVs through O_I by bonding with Ni and Fe sites, and the -OH group continued to shift further away from the OV (IM4). Due to the electron donated from OV to O_I of HSO_5^-, the O_I-O_{II} bond was elongated in IM5, which was radicalized in TS2 to form a transient state and broken to spontaneously produce $SO_4^{\bullet-}$, which absorbed on the surface. The higher energy barrier (ΔE_2) of 1.96 eV than ΔE_1 (0.73 eV) indicated the generation of $SO_4^{\bullet-}$ was the speed-limiting step of the entire reaction. Interestingly, the detached $SO_4^{\bullet-}$ was finally absorbed on another unsaturated Fe site in OV through O_{II} (IM6). The phenomenon of surface-absorbed $SO_4^{\bullet-}$ was consistent with previous experimental results on ROS identification. Due to the high density of surface O atoms in perfect crystals, the steric hindrance impeded the bonding of dissociated radicals to the catalyst surface [19]. However, the OVs-containing surface in α-$Ni_{0.2}Fe_{1.8}O_3$ presented an open structure, and the unoccupied unsaturated Fe sites (except for the Ni and Fe sites bonded with O_I) induced by OVs could serve as perfect Lewis-acid sites for the well-stabilization of $SO_4^{\bullet-}$ fragment and the minimization of overall surface energy [63]. From TS2 to PC2, the -OH gradually bonded with the Fe sites away from OV and finally absorbed on a Fe site at the edge, which will detach from the surface as OH^- in the actual environment (Eq.4). And the ΔG (−3.58 eV) of RC2 to PC2 evidenced that the process that HSO_5^- replaced the surface -OH was spontaneous, which was consistent with in-situ ATR results.

Besides, the E_{ads} of HSO_5^- (−7.72 eV) was much lower than that of -OH groups (−5.22 eV) and H_2O (−1.66 eV), indicating that the HSO_5^- could be more firmly adsorbed on the metal sites (Fig S14). Additionally, the E_{ads} of PMS on the surface of α-$Ni_{0.2}Fe_{1.8}O_3$ was much lower compared to α-Fe_2O_3 (−6.79 eV) as shown in Fig. 7d. Based on the Bader charge results, 0.698 e could be transferred from α-$Ni_{0.2}Fe_{1.8}O_3$ to the PMS, while it was 0.519 e by α-Fe_2O_3, indicating that the OVs synergized exposed Ni and Fe sites benefited the electron transfer for PMS activation.

In order to give further insight into the effect of OV content on the activation of PMS, DFT calculations were conducted. On the (110) plane of α-$Ni_{0.2}Fe_{1.8}O_3$, different numbers of O atoms were removed from the surface to simulate different content of OVs as shown in Fig. 7e (I-III), and named as 1OV, 2OV and 3OV, respectively. Then the adsorption of PMS on the surface of these structures was explored. As shown in Fig. 7e (IV-VI), the ΔE_{ads} of 1OV, 2OV and 3OV model was − 7.72 eV, − 10.70 eV and − 9.60 eV, respectively, meaning the adsorption processes were spontaneous and the α-$Ni_{0.2}Fe_{1.8}O_3$ with 2OV was most favorable for adsorption of PMS. To further shed light on the intrinsic origin of PMS activation, the density of states (DOS) of the surface metal sites in these models were also investigated as shown in Fig S15 and Fig. 7e (VII-IX). The d-band center is a reliable index to evaluate the catalytic activity of catalysts, which is more favorable for the adsorption of surface electrons when closer to the Fermi level (E_f). As shown in Fig. 7f, different concentration of OVs changes the position of the d-band center of Ni and Fe. Compared with the α-$Ni_{0.2}Fe_{1.8}O_3$ with 1OV and 3OV, the d-band center of Fe 3d and Ni 3d in the 2OV model was closer to E_f, indicating the enhanced reactivity of Fe and Ni sites with PMS [64].

After PMS adsorption, Ni 3d and Fe 3d orbitals in these models had considerable overlaps with the O 2p orbital, suggesting the chemical interaction between catalysts and PMS. And the d-band center of Ni 3d and Fe 3d all exhibited a negative shift after PMS adsorption, indicating
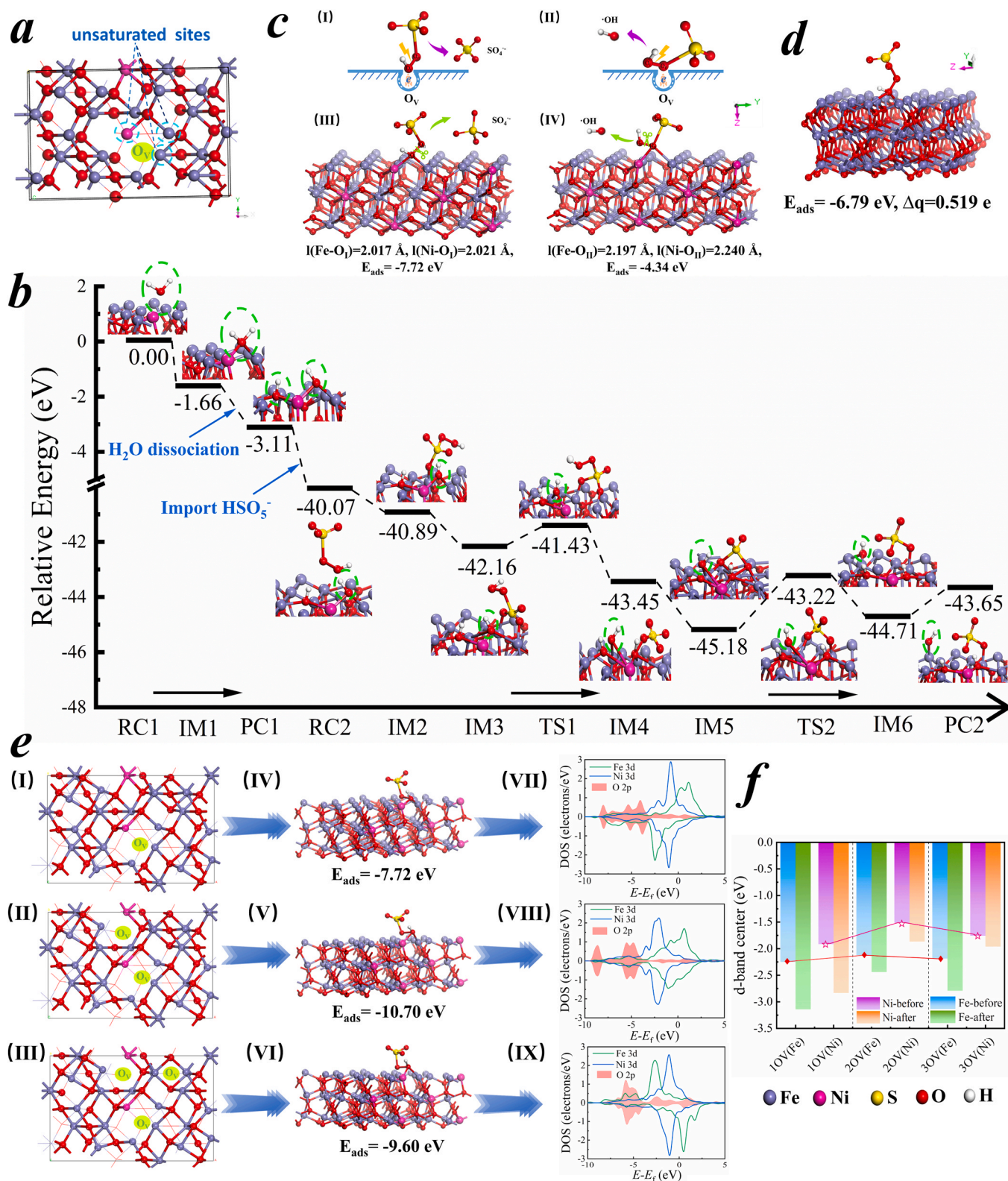
Fig. 7. The sketch map of oxygen vacancy of (110) plane in α-Ni$_{0.2}$Fe$_{1.8}$O$_3$ (a); the bonding process between the catalyst and PMS (b); the sketch map of O$_I$ and O$_{II}$ captured by oxygen vacancy (c$_I$ and c$_{II}$), optimized atomic configurations for revealing adsorption tends of O$_I$ and O$_{II}$ on oxygen vacancy (c$_{III}$ and c$_{IV}$); the adsorption of HSO$_5^-$ on (110) plane in α-Fe$_2$O$_3$ (d); the sketch map (e$_I$ to e$_{III}$), adsorption model of HSO$_5^-$ (e$_{IV}$ to e$_{VI}$) and the partial density of states (PDOS) of Ni 3d, Fe 3d and O 2p (e$_{VII}$-e$_{IX}$) on (110) plane in α-Ni$_{0.2}$Fe$_{1.8}$O$_3$ with different oxygen vacancies; d-band center of Fe and Ni in α-Ni$_{0.2}$Fe$_{1.8}$O$_3$ with different oxygen vacancies before and after PMS adsorption (f).

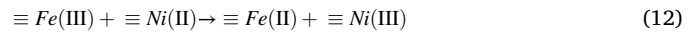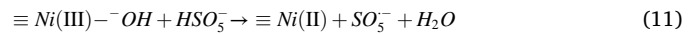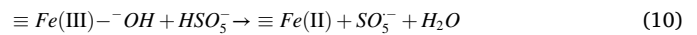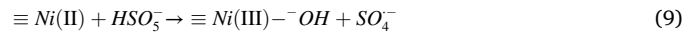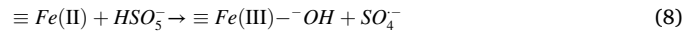that Ni and Fe sites transported electrons to metal-O_I bond [65]. Besides, the d-band center of Fe 3d and Ni 3d in the 2OV model after PMS adsorption was still closer to E_f than others, indicating its stronger reactivity to deepen electron transfer from metal sites to O_I and eventually caused the cleavage of O-O bond to generate $SO_4^{\bullet-}$. In conclusion, appropriate OVs could promote the activation of PMS, and the excess OVs may weaken this boosting effect on the α-$Ni_{0.2}Fe_{1.8}O_3$ surface. This result may explain why excess OVs had little enhancement and even a negative effect on catalytic performance observed in the experimental section.

3.5.3. Insight into activation mechanism

The electron transfer from the Ni and Fe sites to the surface-complexed HSO_5^- was investigated by the deconvolution of the Fe *2p* and Ni *2p* XPS spectra. From Fig. 8a, the peaks at 710.7 and 712.2 eV of Fe $2p_{3/2}$ were assigned to Fe(II) and Fe(III), respectively [66]. The proportion of Fe(II) in the α-$Ni_{0.2}Fe_{1.8}O_3$ decreased from 45.4% to 40.8% after use, and the proportion of Fe(III) correspondingly increased, indicating the donation of the electron from Fe(II) by Fe(II)-O_I to O_I-O_{II}. From Fig. 8b, the peaks at 854.3 eV assigned to Ni(II) and 855.7 eV ascribed to Ni(III) were also changed after the reaction, 3.2% of Ni(III) transferred to Ni(II) [67]. Meanwhile, the content of O_V decreased after the reaction (Fig. 8c-d), which meant the crucial role of it for O adsorption of HSO_5^-. These processes contributed to the reaction 4–5, and thus inducing the cleavage of surface-complexed O_I-O_{II} to form $SO_4^{\bullet-}$ (Eqs. 8–9). Moreover, reactions 10–11 induced the transfer of electrons from the O_I-O_{II} to metal sites, meantime generating $SO_5^{\bullet-}$ with a poor oxidation ability (E_0 =1.1 eV) [68]. The doped Ni^{2+} significantly improved the electrons transfer of α-$Ni_{0.2}Fe_{1.8}O_3$, which may be due to the inner redox between Ni(II)/Ni(III) (E_0 =0.48 eV) and Fe(II)/Fe(III) (E_0 =0.771 eV) [22,69], as Eq. 12. The cycle of the Ni and Fe sites benefitted the activation of surface-complexed HSO_5^-, which was more advantageous compared to monometallic catalysts [8]. $SO_4^{\bullet-}$ could rapidly react with H_2O or OH^- to generate $\bullet OH$ (Eq. 14). Furthermore,

the formation of $O_2^{\bullet-}$ and $^1O_2$ that contributed less to ACF degradation was derived from $SO_4^{\bullet-}$ and $\cdot OH$ (Eqs. 15–18) [70].

$$\equiv Fe(II) + HSO_5^- \rightarrow \equiv Fe(III) -^- OH + SO_4^{\bullet-} \tag{8}$$

$$\equiv Ni(II) + HSO_5^- \rightarrow \equiv Ni(III) -^- OH + SO_4^{\bullet-} \tag{9}$$

$$\equiv Fe(III) -^- OH + HSO_5^- \rightarrow \equiv Fe(II) + SO_5^{\bullet-} + H_2O \tag{10}$$

$$\equiv Ni(III) -^- OH + HSO_5^- \rightarrow \equiv Ni(II) + SO_5^{\bullet-} + H_2O \tag{11}$$

$$\equiv Fe(III) + \equiv Ni(II) \rightarrow \equiv Fe(II) + \equiv Ni(III) \tag{12}$$

$$2SO_5^{\bullet-} + 2H_2O \rightarrow 2O_2 + 2SO_4^{\bullet-} + 4H^+ \tag{13}$$

$$SO_4^{\bullet-} + H_2O \rightarrow SO_4^{2-} + \cdot OH + H^+ \tag{14}$$

$$HSO_5^- + H_2O \rightarrow SO_4^{2-} + H_2O_2 \tag{15}$$

$$H_2O_2 + \cdot OH \rightarrow HO_2 \cdot + H_2O \tag{16}$$

$$HO_2 \cdot \rightarrow O_2^{\bullet-} + H^+ \tag{17}$$

$$HSO_5^- + SO_5^{2-} \rightarrow SO_4^{2-} + HSO_4^- +^1 O_2 \tag{18}$$

$$ROS + ACF \rightarrow \ldots \rightarrow CO_2 + H_2O \tag{19}$$

In general, the redox of Ni(II)/Ni(III) and Fe(II)/Fe(III) dominated the generation of ROS. From Fig. 8e, the H_2-TPR spectra showed that the H_2 consumption of α-$Ni_{0.2}Fe_{1.8}O_3$ started approximately 120 °C earlier than α-Fe_2O_3, indicating that the substitution of Ni(II) made the Fe(III) easier to be reduced to Fe(II) [71]. The substitution of Ni expedites the redox cycle of Fe(III)/Fe(II) in α-$Ni_{0.2}Fe_{1.8}O_3$ for surface-complexed PMS activation, thus improving its catalytic performance. To further validate the role of exposed metal sites, the surface complex process of HSO_5^- with metal sites was obstructed by a pre-treating of α-$Ni_{0.2}Fe_{1.8}O_3$ in the citric
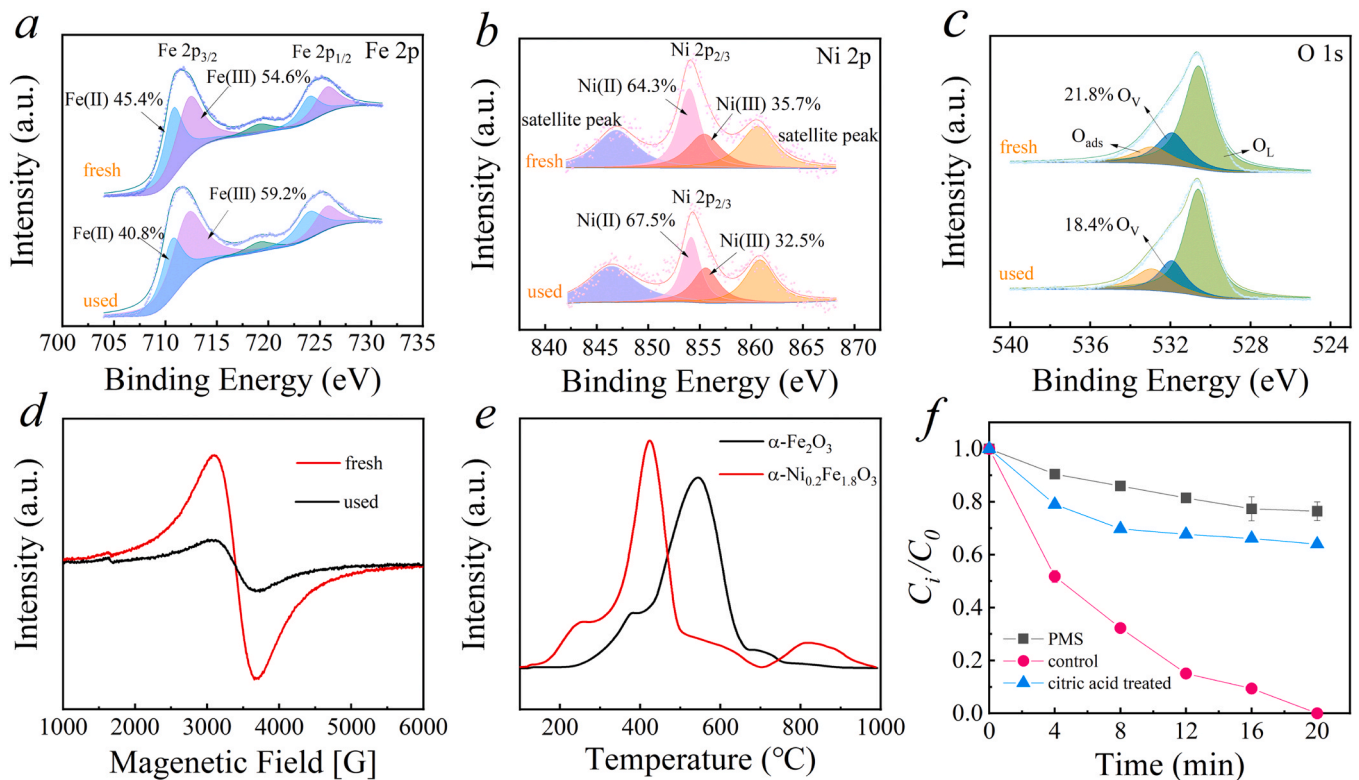
Fig. 8. XPS spectra of Fe 2p, Ni 2p and O 1s in fresh and used α-$Ni_{0.2}Fe_{1.8}O_3$ (a, b, c), ESR spectra of fresh and used α-$Ni_{0.2}Fe_{1.8}O_3$ (d), H_2-TPR spectra of α-Fe_2O_3 and α-$Ni_{0.2}Fe_{1.8}O_3$ (e), degradation of ACF by citric acid untreated and treated α-$Ni_{0.2}Fe_{1.8}O_3$ activating PMS (f).

acid solution to complex Ni and Fe sites [72]. From Fig. 8f, only 36% of ACF was removed by the treated α-Ni$_{0.2}$Fe$_{1.8}$O$_3$ activating PMS, indicating the obstruction of the formation of surface-complexed Me^{n+}-(OH) OSO$_3^-$ caused the inhibition of the reactions proposed.

3.6. Degradation intermediates of ACF

The degradation intermediates of ACF in α-Ni$_{0.2}$Fe$_{1.8}$O$_3$/PMS system were identified by UPLC-QTOF/MS in negative modes, and seventeen

intermediates were detected via controlling a mass error of 5 ppm (details are listed in Table S8 and Fig. S16-19). The possible reaction site on the structure of ACF and its intermediates was speculated by the highest occupied molecular orbital (HOMO) and lowest unoccupied molecular orbital (LUMO) calculation, and the bond orders were also considered [73].

From Fig. 9a and Table S9, according to the results calculated of ACF structure, the bond orders of 1(Cl)− 17(C) and 2(Cl)− 18(C) were relatively lower than others, indicating that the dechlorination reaction

Fig. 9. Wiberg bond order of ACF calculated by the Gaussian with B3LYP/6–31 G basis set, and red number is Wiberg bond order (a), HOMO spectra of ACF (b), distributions of electrostatic potential (ESP) for ACF configuration (c), proposed pathways for the degradation of ACF in the α-Ni$_{0.2}$Fe$_{1.8}$O$_3$/PMS system (d).
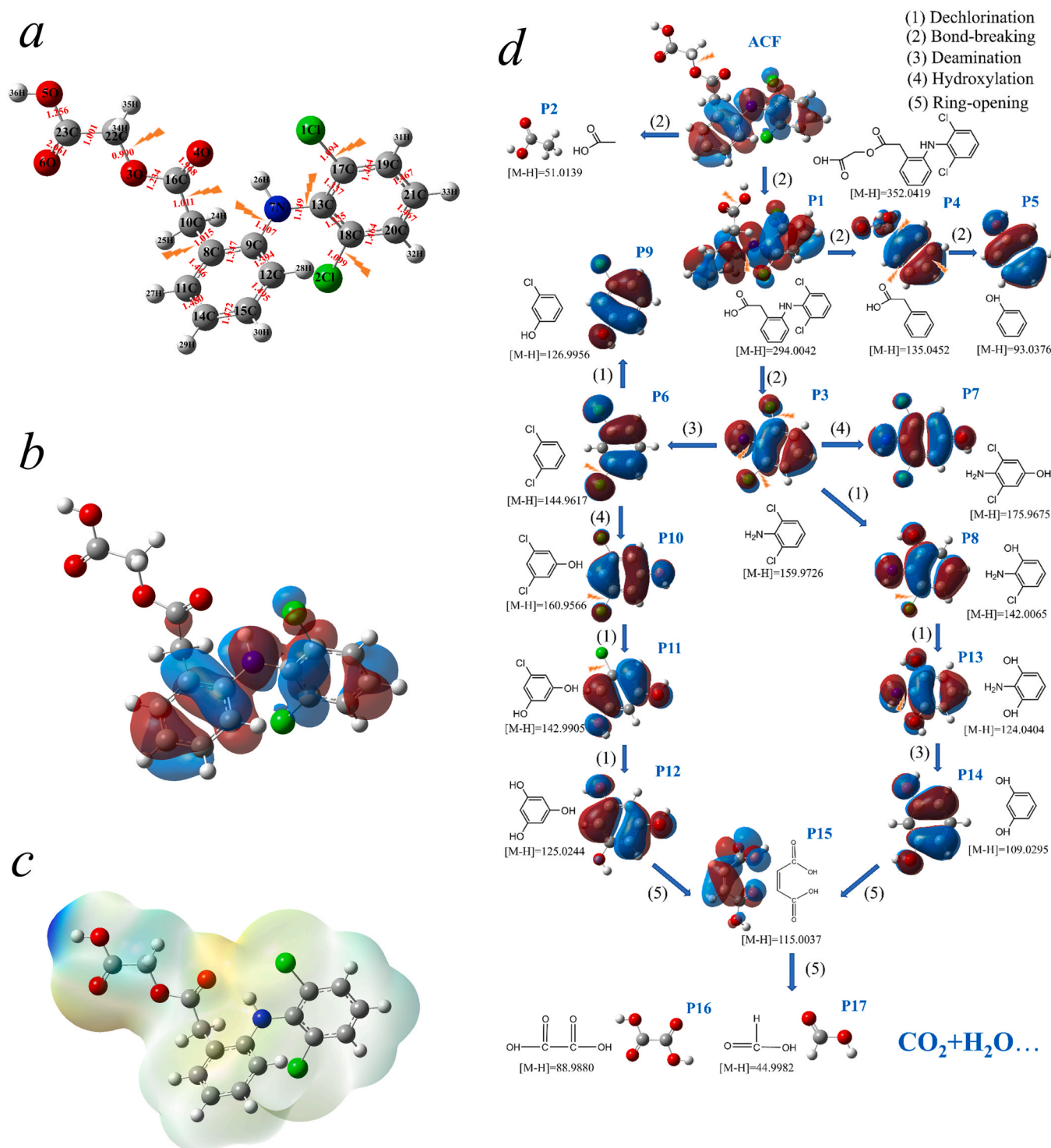
was most likely to occur in the degradation process of ACF (pathway 1). Moreover, the bond of 7(N)− 13(C) and 7(N)− 9(C) was also readily broken, which might cause ACF to decompose into two compounds with a single benzene ring structure and further induced deamination reaction. The similar cleavage of 3(O)− 22(C) and 8(C)− 10(C) also possibly occurred (pathway 2). Frontier orbital theory was also employed to predict the relative activity of individual atomic sites in electrophilic or nucleophilic substitution reactions. From Fig. 9b-c, it can be seen that the HOMO and the distributions of electrostatic potential (ESP) of ACF configuration were mainly located on the N atom, Cl atoms and benzene ring structures, which were more likely attacked by electrophilic reagents, thus inducing deamination reaction (pathway 3), hydroxylation reaction (pathway 4) and opening of the benzene ring (pathway 5). The stepwise generation of P1, P2, P3, P4 and P5 was caused by the cleavage of the bond of 3(O)− 22(C), 7(N)− 9(C) and 8(C)− 10(C) with lower bond orders, respectively. P6 and P7 were generated from P3 by deamination reaction and hydroxylation reaction, respectively. And the further hydroxylation of P6 produced P10. Moreover, P8, P9, P11, P12 and P13 were generated by dechlorination which was caused by the reaction of hydroxyl substitution of -Cl. P14 was produced by the deamination reaction from P13. P15 was mainly generated from the opening reaction of the benzene ring, which eventually degraded to small molecular acids such as glycolic acid (P16) and formic acid (P17) as shown in Fig. 9d.

4. Conclusions

Overall, α-Ni$_{0.2}$Fe$_{1.8}$O$_3$ rich in OVs possesses excellent performance in activating PMS for ACF degradation ($\sim$100%). The constructed α-Ni$_{0.2}$Fe$_{1.8}$O$_3$/PMS system performed well in a wide range of pH (3.0–11.0) and temperature (15–35 ℃). Meanwhile, it presented excellent stability with negligible leaching ions and adaptability for actual water purification. The superior behavior of α-Ni$_{0.2}$Fe$_{1.8}$O$_3$ benefitted from the favorable complexation situation mediated by OVs. The in-situ ATR and Raman analysis revealed the surface-bonding of PMS (Me^{n+}-(HO)OSO$_3$) on the surface metal sites of α-Ni$_{0.2}$Fe$_{1.8}$O$_3$ by the replacement of the surface dissociated -OH groups. The DFT results evidenced that the surface OVs prompted that process and improved the electron transfer compared to α-Fe$_2$O$_3$. The transfer of electrons from Ni or Fe sites via the complexed O-O bond inner the Me^{n+}-(HO)OSO$_3$ induced the activation of surface-complexed HSO$_5^-$. This process prompted the cycle of Ni^{2+}/Ni^{3+} and Fe^{2+}/Fe^{3+}, thus ensuring the long-lasting activation of PMS during application. Based on the results of in situ tests and DFT simulation, the behaviors of H$_2$O and HSO$_5^-$ around OVs were evidenced. Nevertheless, more direct and effective experimental methods that close the actual reaction circumstance should be developed to reveal the interfacial process and give direct guidance for DFT calculation, which is relatively limited in simulating the actual water environment.

CRediT authorship contribution statement

Shuyu Wang: Designed the study, performed the experiments, Data analysis, Writing – original draft preparation. **Jing Kang:** Investigation. **Pengwei Yan:** Conceptualization, Supervision, Project administration, Writing – review & editing. **Jimin Shen:** Detection, Conceptualization. **Jinxiang Zuo** and **Yizhen Cheng:** Validation. **Linlu Shen:** Formal analysis. **Binyuan Wang and Shengxin Zhao:** Detection, Conceptualization. **Zhonglin Chen:** Resources, Project administration.

Declaration of Competing Interest

We declare that we have no financial and personal relationships with other people or organizations that can inappropriately influence our work, and there is no professional or other personal interest of any nature or kind in any product, service and/or company that could be

construed as influencing the position presented in, or the review of, the manuscript entitled, "Surface oxygen vacancy enhanced the activation of peroxymonosulfate on α-Ni$_{0.2}$Fe$_{1.8}$O$_3$ for water decontamination: The overlooked role of H$_2$O in interface mechanism".

Data Availability

Data will be made available on request.

Appendix A. Supporting information

Supplementary data associated with this article can be found in the online version at doi:10.1016/j.apcatb.2023.123419.

References

[1] Y. Wang, X. Zhao, D. Cao, Y. Wang, Y. Zhu, Peroxymonosulfate enhanced visible light photocatalytic degradation bisphenol A by single-atom dispersed Ag mesoporous g-C$_3$N$_4$ hybrid, Appl. Catal. B: Environ. 211 (2017) 79–88, https://doi.org/10.1016/j.apcatb.2017.03.079.

[2] J. Sharma, I.M. Mishra, D.D. Dionysiou, V. Kumar, Oxidative removal of Bisphenol A by UV-C/peroxymonosulfate (PMS): kinetics, influence of co-existing chemicals and degradation pathway, Chem. Eng. J. 276 (2015) 193–204, https://doi.org/10.1016/j.cej.2015.04.021.

[3] L. Yin, J. Wei, Y. Qi, Z. Tu, R. Qu, C. Yan, Z. Wang, F. Zhu, Degradation of pentachlorophenol in peroxymonosulfate/heat system: kinetics, mechanism, and theoretical calculations, Chem. Eng. J. 434 (2022), 134736, https://doi.org/10.1016/j.cej.2022.134736.

[4] X. Lou, C. Fang, Z. Geng, Y. Jin, D. Xiao, Z. Wang, J. Liu, Y. Guo, Significantly enhanced base activation of peroxymonosulfate by polyphosphates: kinetics and mechanism, Chemosphere 173 (2017) 529–534, https://doi.org/10.1016/j.chemosphere.2017.01.093.

[5] Y. Zhen, S. Zhu, Z. Sun, Y. Tian, Z. Li, C. Yang, J. Ma, Identifying the persistent free radicals (PFRs) formed as crucial metastable intermediates during peroxymonosulfate (pms) activation by n-doped carbonaceous materials, Environ. Sci. Technol. 55 (2021) 9293–9304, https://doi.org/10.1021/acs.est.1c01974.

[6] W.-D. Oh, Z. Dong, T.-T. Lim, Generation of sulfate radical through heterogeneous catalysis for organic contaminants removal: current development, challenges and prospects, Appl. Catal. B: Environ. 194 (2016) 169–201, https://doi.org/10.1016/j.apcatb.2016.04.003.

[7] Z. Wang, W. Qiu, S. Pang, Y. Gao, Y. Zhou, Y. Cao, J. Jiang, Relative contribution of ferryl ion species (Fe(IV)) and sulfate radical formed in nanoscale zero valent iron activated peroxydisulfate and peroxymonosulfate processes, Water Res 172 (2020), 115504, https://doi.org/10.1016/j.watres.2020.115504.

[8] N.S. Shah, J.A. Khan, M. Sayed, M. Iqbal, Z.U.H. Khan, N. Muhammad, K. Polychronopoulou, S. Hussain, M. Imran, B. Murtaza, M. Usman, I. Ismail, A. Shafique, F. Howari, Y. Nazzal, Nano-zerovalent copper as a Fenton-like catalyst for the degradation of ciprofloxacin in aqueous solution, J. WATER PROCESS ENG 37 (2020), 101325, https://doi.org/10.1016/j.jwpe.2020.101325.

[9] S. Shao, X. Li, Z. Gong, B. Fan, J. Hu, J. Peng, K. Lu, S. Gao, A new insight into the mechanism in Fe3O4@CuO/PMS system with low oxidant dosage, Chem. Eng. J. 438 (2022), 135474, https://doi.org/10.1016/j.cej.2022.135474.

[10] M. Kohantorabi, G. Moussavi, P. Oulego, S. Giannakis, Heterogeneous catalytic ozonation and peroxone-mediated removal of Acetaminophen using natural and modified hematite-rich soil, as efficient and environmentally friendly catalysts, Appl. Catal. B: Environ. 301 (2022), 120786, https://doi.org/10.1016/j.apcatb.2021.120786.

[11] Y. Ma, B. Wang, Q. Wang, S. Xing, Facile synthesis of α-FeOOH/γ-Fe$_2$O$_3$ by a pH gradient method and the role of γ-Fe$_2$O$_3$ in H$_2$O$_2$ activation under visible light irradiation, Chem. Eng. J. 354 (2018) 75–84, https://doi.org/10.1016/j.cej.2018.08.011.

[12] A. Özcan, A. Atılır Özcan, Y. Demirci, E. Şener, Preparation of Fe$_2$O$_3$ modified kaolin and application in heterogeneous electro-catalytic oxidation of enoxacin, Appl. Catal. B: Environ. 200 (2017) 361–371, https://doi.org/10.1016/j.apcatb.2016.07.018.

[13] N. Wang, Y. Du, W. Ma, P. Xu, X. Han, Rational design and synthesis of SnO$_2$-encapsulated α-Fe$_2$O$_3$ nanocubes as a robust and stable photo-Fenton catalyst, Appl. Catal. B: Environ. 210 (2017) 23–33, https://doi.org/10.1016/j.apcatb.2017.03.037.

[14] X. Li, Z. Wang, B. Zhang, A.I. Rykov, M.A. Ahmed, J. Wang, Fe$_x$Co$_{3-x}$O$_4$ nanocages derived from nanoscale metal–organic frameworks for removal of bisphenol A by

activation of peroxymonosulfate, Appl. Catal. B: Environ. 181 (2016) 788–799, https://doi.org/10.1016/j.apcatb.2015.08.050.

[15] H. Xu, Y. Hu, D. Huang, Y. Lin, W. Zhao, Y. Huang, S. Zhang, Y. Tong, Glucose-induced formation of oxygen vacancy and Bi-Metal comodified Bi₅O₇Br nanotubes for efficient performance photocatalysis, ACS Sustain. Chem. Eng. 7 (2019) 5784–5791, https://doi.org/10.1021/acssuschemeng.8b05336.

[16] G.G. Khan, S. Ghosh, A. Sarkar, G. Mandal, G.D. Mukherjee, U. Manju, N. Banu, B. N. Dev, Defect engineered d⁰ ferromagnetism in tin-doped indium oxide nanostructures and nanocrystalline thin-films, J. Appl. Phys. 118 (2015), 074303, https://doi.org/10.1063/1.4928952.

[17] G. Liu, T. Wang, S. Ouyang, L. Liu, H. Jiang, Q. Yu, T. Kako, J. Ye, Band-structure-controlled BiO(ClBr)(1−x)/2Ix solid solutions for visible-light photocatalysis, J. Mater. Chem. A 3 (2015) 8123–8132, https://doi.org/10.1039/C4TA07128J.

[18] Q. Shao, S. Wei, X. Hu, H. Dong, T. Wen, L. Gao, C. Long, Tuning the micro-coordination environment of Al in dealumination Y zeolite to enhance electron transfer at the Cu–Mn oxides interface for highly efficient catalytic ozonation of toluene at low temperatures, Environ. Sci. Technol. 56 (2022) 15449–15459, https://doi.org/10.1021/acs.est.2c05766.

[19] H. Li, J. Shang, Z. Yang, W. Shen, Z. Ai, L. Zhang, Oxygen vacancy associated surface fenton chemistry: surface structure dependent hydroxyl radicals generation and substrate dependent reactivity, Environ. Sci. Technol. 51 (2017) 5685–5694, https://doi.org/10.1021/acs.est.7b00040.

[20] S. Ndayiragije, Y. Zhang, Y. Zhou, Z. Song, N. Wang, T. Majima, L. Zhu, Mechanochemically tailoring oxygen vacancies of MnO₂ for efficient degradation of tetrabromobisphenol A with peroxymonosulfate, Appl. Catal. B: Environ. 307 (2022), 121168, https://doi.org/10.1016/j.apcatb.2022.121168.

[21] L. Qin, H. Ye, C. Lai, S. Liu, X. Zhou, F. Qin, D. Ma, B. Long, Y. Sun, L. Tang, M. Yan, W. Chen, W. Chen, L. Xiang, Citrate-regulated synthesis of hydrotalcite-like compounds as peroxymonosulfate activator - Investigation of oxygen vacancies and degradation pathways by combining DFT, Appl. Catal. B: Environ. 317 (2022), 121704, https://doi.org/10.1016/j.apcatb.2022.121704.

[22] S. Guo, H. Wang, W. Yang, H. Fida, L. You, K. Zhou, Scalable synthesis of Ca-doped α-Fe₂O₃ with abundant oxygen vacancies for enhanced degradation of organic pollutants through peroxymonosulfate activation, Appl. Catal. B: Environ. 262 (2020), 118250, https://doi.org/10.1016/j.apcatb.2019.118250.

[23] C. Li, Y. Huang, X. Dong, Z. Sun, X. Duan, B. Ren, S. Zheng, D.D. Dionysiou, Highly efficient activation of peroxymonosulfate by natural negatively-charged kaolinite with abundant hydroxyl groups for the degradation of atrazine, Appl. Catal. B: Environ. 247 (2019) 10–23, https://doi.org/10.1016/j.apcatb.2019.01.079.

[24] D. Lu, T. Zhang, L. Gutierrez, J. Ma, J.-P. Croué, Influence of surface properties of filtration-layer metal oxide on ceramic membrane fouling during ultrafiltration of oil/water emulsion, Environ. Sci. Technol. 50 (2016) 4668–4674, https://doi.org/10.1021/acs.est.5b04151.

[25] X. Zhou, A. Jawad, M. Luo, C. Luo, T. Zhang, H. Wang, J. Wang, S. Wang, Z. Chen, Z. Chen, Regulating activation pathway of Cu/persulfate through the incorporation of unreducible metal oxides: pivotal role of surface oxygen vacancies, Appl. Catal. B: Environ. 286 (2021), 119914, https://doi.org/10.1016/j.apcatb.2021.119914.

[26] J. Wei, D. Han, J. Bi, J. Gong, Fe-doped ilmenite CoTiO₃ for antibiotic removal: electronic modulation and enhanced activation of peroxymonosulfate, Chem. Eng. J. 423 (2021), 130165, https://doi.org/10.1016/j.cej.2021.130165.

[27] S. Guo, M. Liu, L. You, G. Cheng, J. Li, K. Zhou, Oxygen vacancy induced peroxymonosulfate activation by Mg-doped Fe₂O₃ composites for advanced oxidation of organic pollutants, Chemosphere 279 (2021), 130482, https://doi.org/10.1016/j.chemosphere.2021.130482.

[28] Y.M. Zhang, S. Yang, J.R.G. Evans, Revisiting Hume-Rothery's rules with artificial neural networks, Acta Mater. 56 (2008) 1094–1105, https://doi.org/10.1016/j.actamat.2007.10.059.

[29] P. Yan, J. Shen, Y. Zhou, L. Yuan, J. Kang, S. Wang, Z. Chen, Interface mechanism of catalytic ozonation in an α-Fe₀.₉Mn₀.₁OOH aqueous suspension for the removal of iohexol, Appl. Catal. B: Environ. 277 (2020), 119055, https://doi.org/10.1016/j.apcatb.2020.119055.

[30] P. Cai, J. Zhao, X. Zhang, T. Zhang, G. Yin, S. Chen, C.-L. Dong, Y.-C. Huang, Y. Sun, D. Yang, B. Xing, Synergy between cobalt and nickel on NiCo₂O₄ nanosheets promotes peroxymonosulfate activation for efficient norfloxacin degradation, Appl. Catal. B: Environ. 306 (2022), 121091, https://doi.org/10.1016/j.apcatb.2022.121091.

[31] J. Yang, P. Li, X. Duan, D. Zeng, Z. Ma, S. An, L. Dong, W. Cen, Y. He, Insights into the role of dual reaction sites for single Ni atom Fenton-like catalyst towards degradation of various organic contaminants, J. Hazard. Mater. 430 (2022), https://doi.org/10.1016/j.jhazmat.2022.128463.

[32] P. Sathishkumar, R.A.A. Meena, T. Palanisami, V. Ashokkumar, T. Palvannan, F. L. Gu, Occurrence, interactive effects and ecological risk of diclofenac in environmental compartments and biota - a review, Sci. Total Environ. 698 (2020), 134057, https://doi.org/10.1016/j.scitotenv.2019.134057.

[33] T.H. Galligan, M.A. Taggart, R.J. Cuthbert, D. Svobodova, J. Chipangura, D. Alderson, V.M. Prakash, V. Naidoo, Metabolism of aceclofenac in cattle to vulture-killing diclofenac, Conserv. Biol. 30 (2016) 1122–1127, https://doi.org/10.1111/cobi.12711.

[34] S. Schmidt, H. Hoffmann, L.-A. Garbe, R.J. Schneider, Liquid chromatography–tandem mass spectrometry detection of diclofenac and related compounds in water samples, J. Chromatogr. A 1538 (2018) 112–116, https://doi.org/10.1016/j.chroma.2018.01.037.

[35] T. Lu, F. Chen, Multiwfn: a multifunctional wavefunction analyzer, J. COMPUT. CHEM 33 (2012) 580–592, https://doi.org/10.1002/jcc.22885.

[36] S. Zuo, D. Li, Z. Guan, F. Yang, H. Xu, D. Xia, J. Wan, Tailored d-band facilitating in Fe Gradient Doping CuO boosts peroxymonosulfate activation for high efficiency

[37] H. Jin, X. Tian, Y. Nie, Z. Zhou, C. Yang, Y. Li, L. Lu, Oxygen vacancy promoted heterogeneous fenton-like degradation of ofloxacin at pH 3.2–9.0 by Cu substituted magnetic Fe₃O₄@FeOOH nanocomposite, Environ. Sci. Technol. 51 (2017) 12699–12706, https://doi.org/10.1021/acs.est.7b04503.

[38] M. Kitajima, Defects in crystals studied by Raman scattering, Crit. Rev. Solid State Mater. Sci. 22 (1997) 275–349, https://doi.org/10.1080/10408439708241263.

[39] C. Hess, New advances in using Raman spectroscopy for the characterization of catalysts and catalytic reactions, Chem. Soc. Rev. 50 (2021) 3519–3564, https://doi.org/10.1039/D0CS01059F.

[40] S. Zhan, S. Zhang, X. Mi, Y. Zhao, C. Hu, L. Lyu, Efficient fenton-like process for pollutant removal in electron-rich/poor reaction sites induced by surface oxygen vacancy over cobalt–zinc oxides, Environ. Sci. Technol. 54 (2020) 8333–8343, https://doi.org/10.1021/acs.est.9b07245.

[41] G. Ou, Y. Xu, B. Wen, R. Lin, B. Ge, Y. Tang, Y. Liang, C. Yang, K. Huang, D. Zu, R. Yu, W. Chen, J. Li, H. Wu, L.-M. Liu, Y. Li, Tuning defects in oxides at room temperature by lithium reduction, Nat. Commun. 9 (2018), 1302, https://doi.org/10.1038/s41467-018-03765-0.

[42] T. Zhang, H. Zhu, J.-P. Croué, Production of sulfate radical from peroxymonosulfate induced by a magnetically separable CuFe₂O₄ spinel in water: efficiency, stability, and mechanism, Environ. Sci. Technol. 47 (2013) 2784–2791, https://doi.org/10.1021/es304721g.

[43] C. Qi, X. Liu, J. Ma, C. Lin, X. Li, H. Zhang, Activation of peroxymonosulfate by base: Implications for the degradation of organic pollutants, Chemosphere 151 (2016) 280–288, https://doi.org/10.1016/j.chemosphere.2016.02.089.

[44] W. Ren, L. Xiong, X. Yuan, Z. Yu, H. Zhang, X. Duan, S. Wang, Activation of peroxydisulfate on carbon nanotubes: electron-transfer mechanism, Environ. Sci. Technol. 53 (2019) 14595–14603, https://doi.org/10.1021/acs.est.9b05475.

[45] S. Lu, G. Wang, S. Chen, H. Yu, F. Ye, X. Quan, Heterogeneous activation of peroxymonosulfate by LaCo₁−ₓCuₓO₃ perovskites for degradation of organic pollutants, J. Hazard. Mater. 353 (2018) 401–409, https://doi.org/10.1016/j.jhazmat.2018.04.021.

[46] K. Maskaoui, J.L. Zhou, Colloids as a sink for certain pharmaceuticals in the aquatic environment, Environ. Sci. Pollut. Res. 17 (2010) 898–907, https://doi.org/10.1007/s11356-009-0279-1.

[47] S. Pérez, D. Barceló, Fate and occurrence of X-ray contrast media in the environment, Anal. Bioanal. Chem. 387 (2007) 1235–1246, https://doi.org/10.1007/s00216-006-0953-9.

[48] L. Wang, X. Lan, W. Peng, Z. Wang, Uncertainty and misinterpretation over identification, quantification and transformation of reactive species generated in catalytic oxidation processes: a review, J. Hazard. Mater. 408 (2021), 124436, https://doi.org/10.1016/j.jhazmat.2020.124436.

[49] Y. Yao, H. Chen, C. Lian, F. Wei, D. Zhang, G. Wu, B. Chen, S. Wang, Fe, Co, Ni nanocrystals encapsulated in nitrogen-doped carbon nanotubes as Fenton-like catalysts for organic pollutant removal, J. Hazard. Mater. 314 (2016) 129–139, https://doi.org/10.1016/j.jhazmat.2016.03.089.

[50] G.V. Buxton, C.L. Greenstock, W.P. Helman, A.B. Ross, Critical Review of rate constants for reactions of hydrated electrons, hydrogen atoms and hydroxyl radicals (·OH/·O− in aqueous solution, J. Phys. Chem. Ref. Data 17 (1988) 513–886, https://doi.org/10.1063/1.555805.

[51] Y. Guo, J. Long, J. Huang, G. Yu, Y. Wang, Can the commonly used quenching method really evaluate the role of reactive oxygen species in pollutant abatement during catalytic ozonation? Water Res 215 (2022), 118275 https://doi.org/10.1016/j.watres.2022.118275.

[52] Y. Zhang, C. Liu, B. Xu, F. Qi, W. Chu, Degradation of benzotriazole by a novel Fenton-like reaction with mesoporous Cu/MnO₂: Combination of adsorption and catalysis oxidation, Appl. Catal. B: Environ. 199 (2016) 447–457, https://doi.org/10.1016/j.apcatb.2016.06.003.

[53] P. Shao, J. Tian, F. Yang, X. Duan, S. Gao, W. Shi, X. Luo, F. Cui, S. Luo, S. Wang, Identification and regulation of active sites on nanodiamonds: establishing a highly efficient catalytic system for oxidation of organic contaminants, Adv. Funct. Mater. 28 (2018), 1705295, https://doi.org/10.1002/adfm.201705295.

[54] W. Zhao, C. Liang, B. Wang, S. Xing, Enhanced Photocatalytic and Fenton-like Performance of CuOx-Decorated ZnFe₂O₄, ACS Appl. Mater. Interfaces 9 (2017) 41927–41936, https://doi.org/10.1021/acsami.7b14799.

[55] X. Duan, H. Sun, Z. Shao, S. Wang, Nonradical reactions in environmental remediation processes: uncertainty and challenges, Appl. Catal. B: Environ. 224 (2018) 973–982, https://doi.org/10.1016/j.apcatb.2017.11.051.

[56] T. Liu, D. Zhang, K. Yin, C. Yang, S. Luo, J.C. Crittenden, Degradation of thiacloprid via unactivated peroxymonosulfate: the overlooked singlet oxygen oxidation, Chem. Eng. J. 388 (2020), 124264, https://doi.org/10.1016/j.cej.2020.124264.

[57] X. Long, C. Feng, D. Ding, N. Chen, S. Yang, H. Chen, X. Wang, O. Oxygen vacancies-enriched CoFe₂O₄ for peroxymonosulfate activation: The reactivity between radical-nonradical coupling way and bisphenol A, J. Hazard. Mater. 418 (2021), 126357, https://doi.org/10.1016/j.jhazmat.2021.126357.

[58] J.A. Perlinger, R. Venkatapathy, J.F. Harrison, Linear free energy relationships for polyhalogenated alkane transformation by electron-transfer mediators in model aqueous systems, J. Phys. Chem. A 104 (2000) 2752–2763, https://doi.org/10.1021/jp993273t.

[59] C. Tian, C. Dai, X. Tian, Y. Nie, C. Yang, Y. Li, Effects of Lewis acid-base site and oxygen vacancy in MgAl minerals on peroxymonosulfate activation towards sulfamethoxazole degradation via radical and non-radical mechanism, Sep. Purif. Technol. 286 (2022), 120437, https://doi.org/10.1016/j.seppur.2021.120437.

[60] T. Zhang, W. Li, J.-P. Croué, Catalytic ozonation of oxalate with a cerium supported palladium oxide: an efficient degradation not relying on hydroxyl

radical oxidation, Environ. Sci. Technol. 45 (2011) 9339–9346, https://doi.org/10.1021/es202209j.

[61] Y. Li, J. Qi, J. Shen, P. Yan, J. Kang, B. Wang, S. Wang, J. Zuo, Z. Chen, Interface mechanism of peroxymonosulfate activation by cobalt-copper-ferrite nanoparticles mediated by palygorskite for bisphenol S degradation: a dual-path activation mechanism, Chem. Eng. J. 448 (2022), 137609, https://doi.org/10.1016/j.cej.2022.137609.

[62] A. Michaelides, A. Alavi, D.A. King, Different surface chemistries of water on Ru {0001}: from monomer adsorption to partially dissociated bilayers, J. Am. Chem. Soc. 125 (2003) 2746–2755, https://doi.org/10.1021/ja028855u.

[63] H. Li, J. Shang, H. Zhu, Z. Yang, Z. Ai, L. Zhang, Oxygen vacancy structure associated photocatalytic water oxidation of BiOCl, ACS Catal. 6 (2016) 8276–8285, https://doi.org/10.1021/acscatal.6b02613.

[64] Z. Zhao, M. Hu, T. Nie, W. Zhou, B. Pan, B. Xing, L. Zhu, Improved electronic structure from spin-state reconstruction of a heteronuclear fe–co diatomic pair to boost the fenton-like reaction, Environ. Sci. Technol. 57 (2023) 4556–4567, https://doi.org/10.1021/acs.est.2c09336.

[65] S. Zuo, Y. Ding, L. Wu, F. Yang, Z. Guan, S. Ding, D. Xia, X. Li, D. Li, Revealing the synergistic mechanism of the generation, migration and nearby utilization of reactive oxygen species in FeOCl-MOF yolk-shell reactors, Water Res 231 (2023), 119631, https://doi.org/10.1016/j.watres.2023.119631.

[66] Y. Ding, L. Zhu, N. Wang, H. Tang, Sulfate radicals induced degradation of tetrabromobisphenol A with nanoscaled magnetic $CuFe_2O_4$ as a heterogeneous catalyst of peroxymonosulfate, Appl. Catal. B: Environ. 129 (2013) 153–162, https://doi.org/10.1016/j.apcatb.2012.09.015.

[67] C. Li, S. Yang, R. Bian, Y. Tan, X. Dong, N. Zhu, X. He, S. Zheng, Z. Sun, Clinoptilolite mediated activation of peroxymonosulfate through spherical dispersion and oriented array of $NiFe_2O_4$: Upgrading synergy and performance, J. Hazard. Mater. 407 (2021), 124736, https://doi.org/10.1016/j.jhazmat.2020.124736.

[68] B.C. Gilbert, J.K. Stell, Mechanisms of peroxide decomposition: an electron paramagnetic resonance study of the reaction of the peroxomonosulphate anion (HOOSO) with CuI. A marked contrast in behaviour with that of TiIII and FeII, J. Chem. Soc. Faraday Trans. 86 (1990) 3261–3266, https://doi.org/10.1039/FT9908603261.

[69] X. Dong, B. Ren, X. Zhang, X. Liu, Z. Sun, C. Li, Y. Tan, S. Yang, S. Zheng, D. D. Dionysiou, Diatomite supported hierarchical 2D $CoNi_3O_4$ nanoribbons as highly efficient peroxymonosulfate catalyst for atrazine degradation, Appl. Catal. B: Environ. 272 (2020), 118971, https://doi.org/10.1016/j.apcatb.2020.118971.

[70] J. Zuo, B. Wang, J. Kang, P. Yan, J. Shen, S. Wang, D. Fu, X. Zhu, T. She, S. Zhao, Z. Chen, Activation of peroxymonosulfate by nanoscaled $NiFe_2O_4$ magnetic particles for the degradation of 2,4-dichlorophenoxyacetic acid in water: efficiency, mechanism and degradation pathways, Sep. Purif. Technol. 297 (2022), 121459, https://doi.org/10.1016/j.seppur.2022.121459.

[71] Y. Rao, Y. Zhang, F. Han, H. Guo, Y. Huang, R. Li, F. Qi, J. Ma, Heterogeneous activation of peroxymonosulfate by $LaFeO_3$ for diclofenac degradation: DFT-assisted mechanistic study and degradation pathways, Chem. Eng. J. 352 (2018) 601–611, https://doi.org/10.1016/j.cej.2018.07.062.

[72] W. Sun, E. Xiao, T. Xiao, V. Krumins, Q. Wang, M. Häggblom, Y. Dong, S. Tang, M. Hu, B. Li, B. Xia, W. Liu, Response of soil microbial communities to elevated antimony and arsenic contamination indicates the relationship between the innate microbiota and contaminant fractions, Environ. Sci. Technol. 51 (2017) 9165–9175, https://doi.org/10.1021/acs.est.7b00294.

[73] X. Xu, J. Chen, S. Wang, J. Ge, R. Qu, M. Feng, V.K. Sharma, Z. Wang, Degradation kinetics and transformation products of chlorophene by aqueous permanganate, Water Res. 138 (2018) 293–300, https://doi.org/10.1016/j.watres.2018.03.057.